Gas release systematics of mineral-hosted fluid inclusions during stepwise crushing: implications for 40Ar/39Ar geochronology of hydrothermal fluids

Article *in* Geochimica et Cosmochimica Acta · February 2019

DOI: 10.1016/j.gca.2019.02.016

CITATIONS
2

READS
225

8 authors, including:

Ming Xiao
Chinese Academy of Sciences
2 PUBLICATIONS **2** CITATIONS
SEE PROFILE

Huaning Qiu
China University of Geosciences
84 PUBLICATIONS **2,049** CITATIONS
SEE PROFILE

Yingde Jiang
Chinese Academy of Sciences
67 PUBLICATIONS **878** CITATIONS
SEE PROFILE

Yue Cai
Columbia University
47 PUBLICATIONS **677** CITATIONS
SEE PROFILE

Available online at www.sciencedirect.com

ScienceDirect

Geochimica et Cosmochimica Acta 251 (2019) 36–55

Geochimica et Cosmochimica Acta

www.elsevier.com/locate/gca

Gas release systematics of mineral-hosted fluid inclusions during stepwise crushing: implications for $^{40}Ar/^{39}Ar$ geochronology of hydrothermal fluids

Ming Xiao [a,b], Hua-Ning Qiu [c,*], Ying-De Jiang [a,*], Yue Cai [d], Xiu-Juan Bai [c], Wan-Feng Zhang [a], Man Liu [e], Chao-Jian Qin [f]

[a] State Key Laboratory of Isotope Geochronology and Geochemistry, Guangzhou Institute of Geochemistry, Chinese Academy of Sciences, Guangzhou 510640, China

[b] University of Chinese Academy of Sciences, Beijing 10049, China

[c] Key Laboratory of Tectonics and Petroleum Resources, China University of Geosciences (Wuhan), Ministry of Education, Wuhan 430074, China

[d] Lamont-Doherty Earth Observatory of Columbia University, 61 Rt. 9W, Palisades, NY 10964, USA

[e] Geology Team 940 of Nonferrous Metals Bureau of Guangdong Province, Qingyuan 511520, China

[f] State Key Laboratory of Ore Deposit Geochemistry, Institute of Geochemistry, Chinese Academy of Sciences, Guiyang 550081, China

Received 10 August 2018; accepted in revised form 9 February 2019; Available online 15 February 2019

Abstract

$^{40}Ar/^{39}Ar$ stepwise crushing technique has become more important for dating hydrothermal fluids trapped in mineral-hosted fluid inclusions. However, understanding the gas release patterns and interpreting the $^{40}Ar/^{39}Ar$ dating results have remained challenging. Here we use $^{40}Ar/^{39}Ar$ analyses coupled with quadrupole mass spectrometer (QMS) analyses of gases released by stepwise crushing to reconstruct the hydrothermal activities recorded by fluid inclusions hosted by wolframite, cassiterite, and quartz from the Yaogangxian tungsten deposit in South China. Microscopic observations and laser Raman spectroscopic studies reveal two main groups of fluid inclusions hosted in hydrothermal minerals: small, isolated and CH_4-rich primary fluid inclusions (PFIs), and larger, mostly CO_2-rich secondary fluid inclusions (SFIs) that distribute along micro-cracks. Formamide and alkane in the vapor phases of large aqueous SFIs are also found. The QMS analyses reveal systematic compositional features for gases released during different crushing stages: (1) gases from the initial crushing stage are H_2O-poor, CO_2-rich with $CO_2/CH_4 > 1$, likely dominated by gases from large vapor-rich SFIs; (2) gases from the final crushing stage are CH_4-dominated gas mixtures with $CO_2/CH_4 < 1$, likely dominated by gases from small PFIs; while (3) gases from the intermediate stage are rich in H_2O, formamide, and ethane, which resemble gases from large liquid-rich SFIs. Combined results from microscopic observations, and Raman and QMS analyses suggest that stepwise crushing extracts gases progressively from large vapor-rich SFIs, large aqueous SFIs to small PFIs. Similarly, gases released during each crushing stage have distinct $^{40}Ar/^{39}Ar$ compositions and corresponding ages. Gases released during the initial crushing stage show high and correlated $^{40}Ar^*$ and $^{38}Ar_{Cl}$ signals with abnormally old $^{40}Ar/^{39}Ar$ ages, which could be related to the vapor-rich SFIs. Gases released during the final crushing stage yield $^{40}Ar/^{39}Ar$ ages of 159–154 Ma, which agree well with stepwise heating $^{40}Ar/^{39}Ar$ age (156 ± 0.9 Ma) of intergrown muscovite and published ore-forming ages. We propose that the $^{40}Ar/^{39}Ar$ ages of gases released during the final crushing stage are reasonable age estimates for the PFIs. Gases released during the intermediate stage yield $^{40}Ar/^{39}Ar$ ages of 128–127 Ma, which agree well with stepwise heating $^{40}Ar/^{39}Ar$ age (129 ± 2.1 Ma) of the cross-cutting K-feldspar vein. This result likely suggests that intermediate stage gases mainly derived from aqueous SFIs that formed during late-stage hydrothermal events. In this study, we demonstrate that gas release patterns revealed by $^{40}Ar/^{39}Ar$

* Corresponding authors.
E-mail addresses: huaningqiu@cug.edu.cn (H.-N. Qiu), jiangyd@gig.ac.cn (Y.-D. Jiang).

https://doi.org/10.1016/j.gca.2019.02.016

stepwise crushing are consistent with those revealed by Raman and QMS analyses. Therefore, combining these techniques provides a better picture of the timing and nature of hydrothermal geofluids in general.

Keywords: Stepwise crushing; QMS gas analysis; Fluid inclusion $^{40}Ar/^{39}Ar$ geochronology; Gas release patterns; Dating hydrothermal fluids

1. INTRODUCTION

Fluid inclusions, especially primary fluid inclusions preserve crucial information of geological processes, such as pressure-temperature conditions during ore/rock formation and nature, provenance, evolution history as well as ages of geofluids (Shepherd and Darbyshire, 1981; Roedder, 1984; Shepherd et al., 1985; Kelley et al., 1986; Shepherd and Miller, 1988; Roedder, 1992; Pettke et al., 1997; Audétat et al., 1998). Mineral crushing is an effective way to extract gases from fluid inclusions hosted by hydrothermal minerals (Andrawes et al., 1984; Norman and Sawkins, 1987; Norman and Musgrave, 1994; Moore et al., 2001; Camprubí et al., 2006; Blamey, 2012; Azmy and Blamey, 2013). When combined with $^{40}Ar/^{39}Ar$ geochronology, this technique has provided a new way to date hydrothermal deposits (Kelley et al., 1986; Turner, 1988; Qiu and Dai, 1989; Turner and Bannon, 1992; Qiu et al., 2002; Qiu and Jiang, 2007; Bai et al., 2013). $^{40}Ar/^{39}Ar$ crushing technique of mineral-hosted fluid inclusions has overcome several obstacles in constraining the timing of mineralization, for example, (1) often only limited numbers of suitable mineral phases are available for conventional dating methods, i.e., Rb–Sr, Sm–Nd and U–Pb; (2) $^{40}Ar/^{39}Ar$ heating cannot yield precise ages of K-poor minerals; and (3) owing to the ambiguous paragenesis relationship between the gangue and the ore minerals, the ages of gangue minerals cannot fully constrain the timing of mineralization. Directly dating of hydrothermal fluids within primary fluid inclusions trapped in ore minerals during mineral growth could overcome these obstacles and provide additional and perhaps better age constraints for mineralization (e.g., Qiu and Jiang, 2007; Bai et al., 2013; Wang et al., 2015).

Dating fluids is no easy feat. Experimental studies suggest that the gases released during mineral crushing could be mixtures from different reservoirs, e.g., primary and secondary mineral-hosted fluid inclusions, mineral inclusions/impurities as well as gases in mineral micro-cracks and lattices (Villa, 2001; Qiu et al., 2002; Kendrick et al., 2006). Source identification can be challenging and $^{40}Ar/^{39}Ar$ ages of fluid inclusions obtained by crushing could be difficult to interpret. An effective crushing technique that can progressively extract fluid inclusions coupled with clear gas release patterns during mineral crushing is therefore important for identification of gas sources in different crushing stages and obtaining accurate ore-forming information such as the nature, source, and age of the mineralizing fluid.

Stepwise crushing of minerals with gentle force, which will be referred to as gentle stepwise crushing, is a potential way to liberate gases from specific reservoirs (e.g., Bai et al., 2018a). A technique for gentle stepwise crushing of minerals has been established by recent studies (Qiu and Jiang, 2007; Jiang et al., 2012; Bai et al., 2013; Bai et al., 2018a), through free drop of a light pestle from a relatively low dropping height (3–5 cm). These studies show that the first hundred pestle drops (pestle drop number represents the number of times that the pestle was dropped to crush the sample) appear to only release gases from large secondary fluid inclusions along micro-cracks. After about a thousand pestle drops, gases from smaller primary fluid inclusions become more dominant. Meanwhile, gases residing in the crystal lattice are not released until much later. If these assumptions are valid, then gentle stepwise crushing could reveal geochronological information of different generations of fluid inclusions and potentially be used to date different hydrothermal events. Correlations of Ca-, Cl-, and K-derived Ar isotopes that formed during neutron irradiation ($^{37}Ar_{Ca}$, $^{38}Ar_{Cl}$, and $^{39}Ar_{K}$) could also be used to distinguish gases from secondary fluid inclusions from primary ones, and obtain $^{40}Ar/^{39}Ar$ ages of different fluid inclusion groups (Jiang et al., 2012; Bai et al., 2013), which further extends the application of $^{40}Ar/^{39}Ar$ stepwise crushing technique. $^{40}Ar/^{39}Ar$ stepwise crushing technique has been successfully applied to date various geofluids, such as ore-forming fluids (Qiu, 1996; Qiu and Jiang, 2007; Jiang et al., 2012; Bai et al., 2013; Wang et al., 2015), hydrocarbon accumulation geofluids (Qiu et al., 2011) and metamorphic fluids (Qiu and Wijbrans, 2006; Qiu et al., 2010; Hu et al., 2015; Uunk et al., 2017).

So far our understanding of gas release patterns during stepwise crushing mostly comes from the correlations of argon isotopes induced from K, Cl and Ca, which unfortunately cannot be used to reconstruct gas release patterns during stepwise crushing. The compositions of gases released during stepwise crushing experiments contain additional information that could help us constrain potential gas reservoirs and interpret $^{40}Ar/^{39}Ar$ geochronology results. Quadrupole mass spectrometer (QMS) is widely used in fluid inclusion gas composition analyses, owing to its rapid scanning, wide detection range and low detection limit (Norman and Sawkins, 1987; Moore et al., 2001; Camprubí et al., 2006; Blamey, 2012). When coupled with stepwise crushing apparatus (Qiu and Wijbrans, 2006; Qiu and Jiang, 2007; Qiu et al., 2011), QMS can provide new insights into the processes of releasing gases from mineral-hosted fluid inclusions and thus permit a better understanding of fluid inclusion $^{40}Ar/^{39}Ar$ geochronology, including identification of the potential sources of released argon and more accurate interpretations of the $^{40}Ar/^{39}Ar$ ages obtained during stepwise crushing.

Using established gentle stepwise crushing technique (Qiu and Jiang, 2007; Qiu et al., 2011; Bai et al., 2013), we report $^{40}Ar/^{39}Ar$ geochronology and QMS geochemical analyses of stepwise released gases from fluid inclusions

hosted by ore minerals such as wolframite and cassiterite, as well as gangue mineral quartz from the Yaogangxian tungsten deposit, South China. Before processing, microscopic observation, Raman spectroscopy, and carbon isotopic analyses were also performed to constrain the compositions and the sources of the gases and fluids from both primary and secondary fluid inclusions. When integrated with QMS measurements during stepwise mineral crushing, these data provide a better understanding of the $^{40}Ar/^{39}Ar$ ages obtained through the same gas release method. We demonstrate that $^{40}Ar/^{39}Ar$ stepwise crushing technique can be used to date different generations of mineral-hosted fluid inclusions in K-poor minerals that formed during hydrothermal processes.

2. GEOLOGICAL SETTING, SAMPLES AND MINERAL-HOSTED FLUID INCLUSIONS

2.1. Geology of the Yaogangxian tungsten deposit

The South China Block consists of the Yangtze Block in the northwest and the Cathaysia Block in the southeast, which have amalgamated during the Proterozoic (Charvet et al., 1996; Li and Mcculloch, 1996; Li et al., 2009). The Nanling Range (111–117°E, 23°20′–26°40′N), located at the central-southern part of South China, is characterized by widespread granitic magmatism associated with rare-metal mineralization (Shu, 2007), which forms the Nanling polymetallic metallogenic belt (Fig. 1a). Large-scale W-Sn polymetallic mineralization closely associated with the granitic magma developed in the Middle to Late Jurassic in this belt (Mao et al., 2007; Fu et al., 2013), which is associated with a Late Mesozoic intra-continental extensional tectonic setting caused by the subduction of the Paleo-Pacific oceanic plate (Zhou et al., 2006; Shu, 2007). These intra-continental magmatic activities could be triggered by melting of the upper- and middle-crust as a result of increased slab angle generating upwelling of hot asthenospheric material (Zhou and Li, 2000) or back-arc extension following northwestward subduction of the Paleo-Pacific plate (Zhou et al., 2006). Finally, flat subduction model proposed by Li and Li (2007) suggested that the breakoff and delamination of the subducted slab after flat subduction at *ca.* 250–190 Ma induced asthenosphere upwelling, and generated this Late Mesozoic magmatism in the interior of the South China Block.

The Yaogangxian world-class tungsten deposit, situated in the northern part of the Cathaysia Block and the heartland of the Nanling metallogenic belt (Fig. 1), represents the largest tungsten deposit in this region. The tungsten-tin mineralization is spatially and temporally associated with the highly differentiated S-type Yaogangxian granitic intrusion (Chen, 1988; Peng et al., 2006; Li et al., 2015). The estimated timing of tungsten mineralization is 163–153 Ma based on Re–Os dating of molybdenite (Peng et al., 2006; Wang et al., 2010) and $^{40}Ar/^{39}Ar$ stepwise heating of hydrothermal phlogopite and muscovite (Peng et al., 2006). These ages are similar to the crystallization ages of the Yaogangxian granites (158–155 Ma, zircon U–Pb, Li et al., 2011). Additionally, similarities in S–Pb–H–O isotopic compositions of ore/gangue minerals and of magma or magmatic water (Zhang, 1987; Zhu et al., 2014b) also indicated a "genetic" association between the mineralization and the intrusion.

In the mining district, the stratigraphic sequences mainly comprise Cambrian meta-sandstone and slate, Devonian-Carboniferous sandstone and limestone, and Triassic-Jurassic sandstone (Chen, 1981, 1988) (Fig. 1b). Tungsten mineralization developed primarily along the contact zone between the pluton and the sedimentary strata. The ore bodies were mainly emplaced in the Cambrian-Devonian sequences and mainly consist of quartz vein-type wolframite associated with skarn-type scheelite and minor greisen-type wolframite.

The vein-type orebodies are mostly NW-SE striking without showing any evidence of apparent multi-staged mineralization events (Zhu et al., 2014a). A paragenetic sequence that varies across the vein-type mine typically consists of quartz, micas, wolframite and varying quantities of cassiterite, fluorite, and sulfides including molybdenite, arsenopyrite, pyrite, chalcopyrite, and sphalerite. Late K-feldspar veins crosscutting orebodies are widely present (e.g., Fig. 2a).

Multi-stage post-mineralization hydrothermal/structural events have most likely affected the ore deposits in the Nanling region to different extents, as late K-feldspar veins crosscutting the ore bodies prevail in regional metal deposits, e.g., the Caijiaping Pb-Zn deposit (Dai et al., 2011), the Piaotang tungsten deposit (Bai et al., 2013), and the Shizhuyuan W-Sn-Mo-Bi deposit (Wang et al., 2016). Additionally, multiple types of secondary fluid inclusions are present in both ore and gangue minerals in regional ore deposits, which further indicates late-stage hydrothermal disturbances (Giuliani et al., 1988; Bai et al., 2013; Liu et al., 2015; Ni et al., 2015). Fluid inclusion studies of the Yaogangxian tungsten deposit (e.g., Cao et al., 2009; Dong et al., 2011; Yu et al., 2015) suggest that tungsten-bearing ore veins are also characterized by the coexistence of complex multi-generation fluid inclusions without experiencing the fluid boiling phenomenon that can significantly fractionate isotopes (Villa, 2001). Multiple-stage post-mineralization hydrothermal/structural disturbances of this deposit embodied by later K-feldspar veins (Fig. 2a) and the coexistence of primary and secondary fluid inclusions make it an ideal research object for investigating the systematic gas release patterns during stepwise crushing and verifying the ability of $^{40}Ar/^{39}Ar$ stepwise crushing to date different generations of fluid inclusions.

2.2. Samples and fluid inclusions

Here, we focus on the tungsten-tin-bearing quartz veins. Two fresh samples (13YGX06 and 13YGX36) were collected for integrated micro-examination, gas composition analyses, and $^{40}Ar/^{39}Ar$ dating. The samples have similar mineral assemblages that can be characterized by textural intergrowth of ore minerals (e.g., wolframite, cassiterite, and sulfide) with gangue minerals (e.g., quartz and hydrothermal muscovite). Both ore and gangue minerals show no evidence of deformation (Fig. A1, Appendix A).

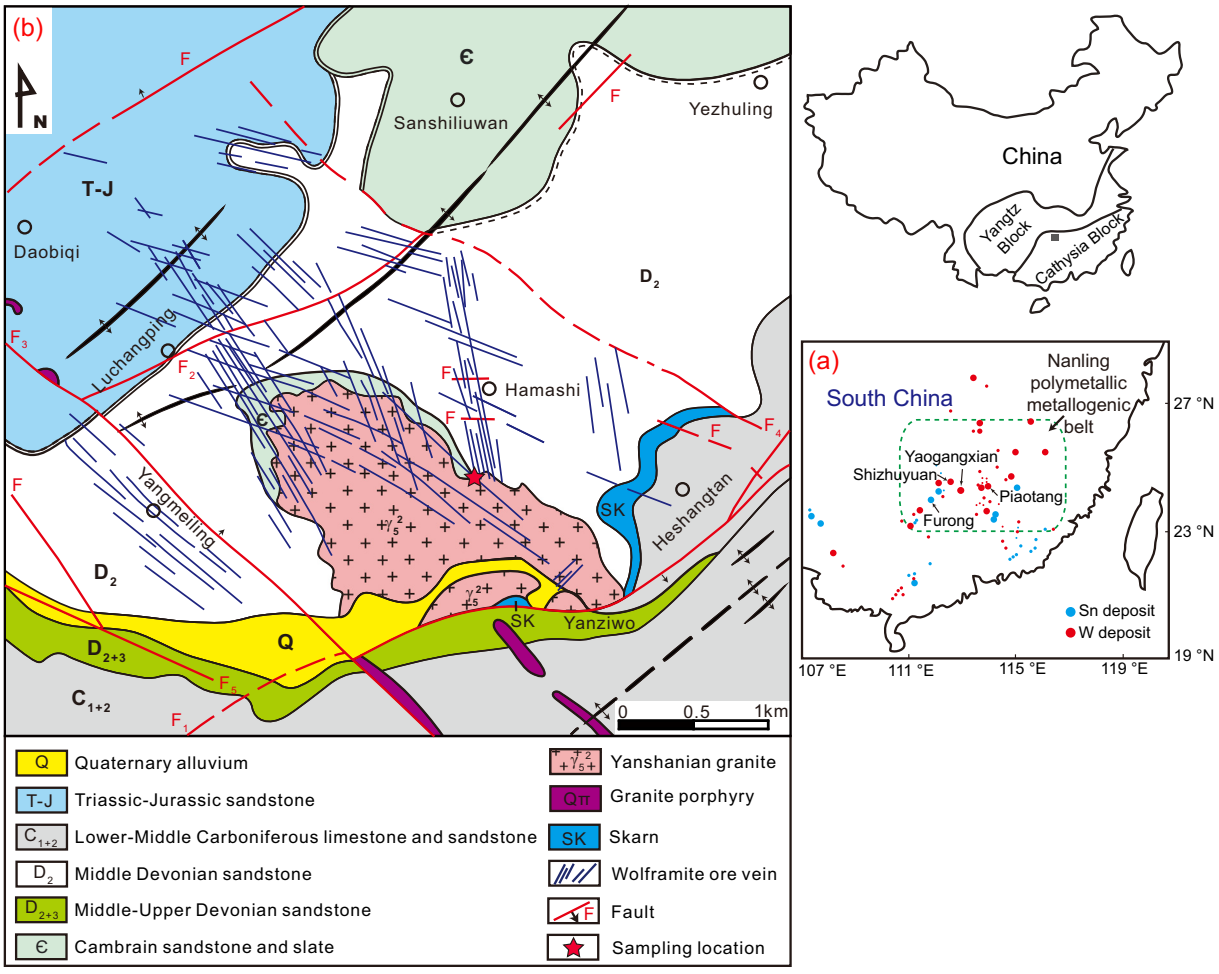

Fig. 1. (a) Geological map showing the distribution of important W-Sn ore deposits in South China (modified after Mao et al. (2011)). (b) Geological map of the Yaogangxian tungsten deposit (modified after Peng et al. (2006) and Zhu et al. (2015)).

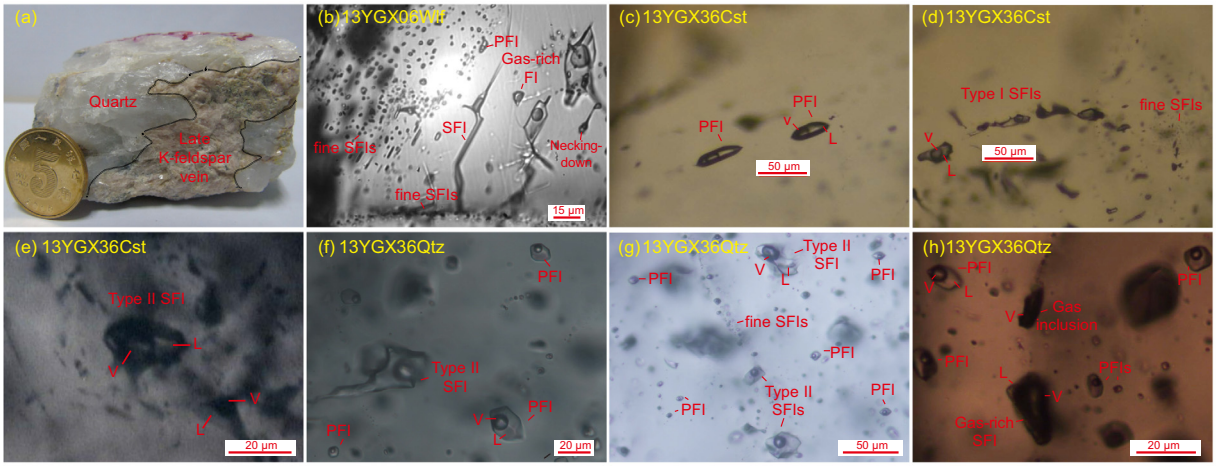

Fig. 2. Petrography of late K-feldspar vein and micrographs of fluid inclusions within the minerals. (a) Late K-feldspar vein crosscuts the quartz vein. (b) Fluid inclusions in wolframite sample 13YGX06Wlf. (c–e) Fluid inclusions in cassiterite sample 13YGX36Cst. (f–h) Fluid inclusions in vein quartz sample 13YGX36Qtz. Photomicrograph of wolframite was taken with a ROLERA-XR infrared digital camera. Abbreviations: Wlf: wolframite, Cst: cassiterite, Qtz: quartz, L: aqueous solution, V: vapor phase, FI: fluid inclusion, PFI: primary fluid inclusion, SFI: secondary fluid inclusion.

Two main generations of fluid inclusions, namely the primary fluid inclusions (PFIs) and the secondary fluid inclusions (SFIs) can be identified within the wolframite, cassiterite and vein quartz based on their morphology at room temperature and distribution, according to the discriminant standard: the PFIs are generally trapped during mineral growth and are isolated or distributed along mineral growth zones/crystal faces with regular shapes, whereas SFIs are generally trapped later than mineral formation and distribute linearly along micro-cracks with irregular shapes (Roedder, 1984; Van Den Kerkhof and Hein, 2001).

The PFIs in the studied minerals are typically bi-phase. They are generally isolated and small in sizes with negative crystal shapes (i.e., the fluid inclusions assume crystal habits of the host minerals, Fig. 2b–h). No late modification such as leakage, shrink, dismemberment and decrepitation (see Van Den Kerkhof and Hein, 2001; Diamond et al., 2010) were observed among these small PFIs. Different from the PFIs, the SFIs distribute along micro-cracks or healed micro-cracks and generally have higher vapor/liquid ratios. The SFIs include aqueous bi-phase SFIs, gas-rich bi-phase SFIs, minor gas inclusions and negligible CO_2-bearing tri-phase SFIs (Fig. 2b–h). Negligible amounts of daughter minerals bearing tri-phase fluid inclusions developed in the studied minerals. Detailed features of fluid inclusions of each mineral type are discussed in Section 4.1.

3. ANALYTICAL METHODS

3.1. Composition of individual fluid inclusion by Raman spectroscopy

Compositions of individual fluid inclusions were analyzed using a Renishaw InVia Reflex micro-Raman spectrometer, equipped with an Ar^+ ion laser (514.5 nm), at State Key Laboratory of Ore Deposit Geochemistry, Institute of Geochemistry, Chinese Academy of Sciences (CAS) with a resolution of $\pm 1\ cm^{-1}$. Several gas species were identified by their Raman spectroscopy: $CO_2 = 1388\ cm^{-1}$, $CH_4 = 2917\ cm^{-1}$, $N_2 = 2329\ cm^{-1}$. The $A(CO_2/CH_4)$ values were calculated as area ratios of the Raman peaks of CO_2 and CH_4 using the software PeakFit (version v.4.12, Singh et al., 2011).

3.2. Fluid inclusion carbon isotope analyses

Five quartz samples (~50 mg of each) were selected from wolframite bearing quartz veins for carbon isotopic analyses using a Finningan MAT 253 mass spectrometer at the Stable Isotope Laboratory of the Institute of Mineral Resources, Chinese Academy of Geological Sciences. The results are reported in conventional δ-values as ‰ deviations relative to the Vienna Pee Dee Belemnite (VPDB) standard with an analytical precision of ±0.2‰. The CO_2 within fluid inclusions was released by decrepitation with a heating temperature of 600 °C. Released CO_2 gas was condensed and collected using a liquid nitrogen-alcohol cold trap for CO_2 carbon isotopes analyses. The remaining CO_2-free gas mixture was transported into a copper-oxide furnace and then heated up to 800 °C in order to convert CH_4 into CO_2 for CH_4 carbon isotopic measurement.

3.3. $^{40}Ar/^{39}Ar$ geochronology of irradiated samples

Three fluid inclusion-rich mineral samples including one wolframite from quartz vein sample 13YGX06, one cassiterite and one vein quartz from quartz vein sample 13YGX36 were selected for stepwise crushing $^{40}Ar/^{39}Ar$ dating. In addition, one muscovite and one K-feldspar sample from the quartz vein sample 13YGX36 were selected for stepwise heating $^{40}Ar/^{39}Ar$ dating.

These mineral samples were wrapped with aluminum foil and then placed in an aluminum vessel together with monitor standard ZBH-2506. ZBH-2506 is a biotite standard with $^{40}Ar/^{39}Ar$ plateau age of 132.7 ± 0.1 Ma (Wang, 1983). The monitor standard was inserted between every two to four samples, for irradiation *J*-value calculation.

The $^{40}Ar/^{39}Ar$ dating was conducted at MOE Key Laboratory of Tectonics and Petroleum Resources, China University of Geosciences (Wuhan) (Bai et al., 2018b). The stepwise crushing experiments were carried out using an in-house designed crushing system (Qiu and Wijbrans, 2006; Qiu and Jiang, 2007; Qiu et al., 2011; Jiang et al., 2012). The stepwise heating experiments were carried out using a 50 W CO_2 laser. The released gases were cleaned through a series of steps, first through a cryotrap at −110 °C, which is followed by equilibration with a SAES Zr/Al getter at room temperature and another Zr/Al getter at 400 °C for 400 seconds.

The purified noble gases were then analyzed by an ARGUS VI® mass spectrometer. The *J*-value of each sample was interpolated based on the regression line of *J*-values of measured monitor standards. $^{40}Ar/^{39}Ar$ data are calculated and plotted using the software ArArCALC (version 2.5.2, Koppers, 2002). The total decay constant for ^{40}K used is $\lambda = 5.543 \times 10^{-10}$/yr from Steiger and Jäger (1977). The correction factors used for interfering argon isotopes derived from irradiated CaF_2 and K_2SO_4 are: $(^{39}Ar/^{37}Ar)_{Ca} = 6.175 \times 10^{-4}$, $(^{36}Ar/^{37}Ar)_{Ca} = 2.348 \times 10^{-4}$ and $(^{40}Ar/^{39}Ar)_K = 2.323 \times 10^{-3}$.

3.4. Quadrupole mass spectrometer gas analyses of unirradiated samples

In addition to $^{40}Ar/^{39}Ar$ analyses, the unirradiated counterparts of wolframite sample 13YGX06Wlf, cassiterite sample 13YGX36Cst and vein quartz sample 13YGX36Qtz were also measured using a quadrupole mass spectrometer (QMS) in a separate but similar stepwise crushing experiment in order to investigate the compositions of extracted gas during stepwise crushing.

The QMS gas analysis system was recently designed and installed by H. N. Qiu, which consists of a crusher (almost identical as the $^{40}Ar/^{39}Ar$ crusher), an SRS© RGA200® QMS and a Pfeiffer HiCube80 Eco® turbo pumping station. Two SAES NP10® getters were installed within the QMS line with an isolating valve. The RGA200 QMS is equipped

with a faraday and an electron multiplier. The QMS has a mass range of 1 to 200 amu.

The improved crusher consists of a type 316L stainless steel tube (length: 160 mm, inner diameter: 28 mm) with a spherical curvature on the internal base, and a magnetic 3Cr13 type (or S42030) stainless steel pestle with a weight of 214 g. An external electric magnet with a frequency of 2.5 Hz that is controlled by an adjustable repeating-timer-relay was used to repeatedly lift and drop the pestle to crush the mineral samples at the bottom of the crushing tube. The crushing strength of this crusher is more than an order of magnitude lower than the traditional air-actuated *in vacuo* crushing device based on the design of Matsumoto et al. (2001). The lower crushing strength is employed to release gas from fluid inclusions instead of mineral lattice to constrain the timing of hydrocarbon accumulation or mineralization (e.g., Qiu et al., 2011; Jiang et al., 2012; Bai et al., 2013; Bai et al., 2018a).

The mineral samples of 250–840 μm in size were carefully hand-picked under a binocular microscope to ensure a high grade of purity. Samples were rinsed several times with dilute nitric acid and deionized water in an ultrasonic bath to remove surface organics. The QMS gas analyses were performed using a similar crushing system as the $^{40}Ar/^{39}Ar$ crushing experiment. About 150 mg of the mineral sample was loaded into the bottom of the crushing tube. The crusher system was baked out at 150 °C using a furnace and the connecting tubes were baked at 200 °C using heating tapes for 20 hours.

Prior to the crushing experiments, the whole system was pumped by the turbo pump and then the isolating valve was opened to the SAES NP10® getters in order to achieve an ultra-high vacuum condition (better than 4.0×10^{-8} mbar). During the crushing experiments, the getters were blocked, and the turbo pump was used only to clean the system after each measurement. The crushing experiment was performed at room temperature. A blank measurement was carried out before every extraction to quantify the blank contributions of the line. The blank was measured in a static state without the movement of the pestle rather than crushing an empty tube because the latter could generate a significant amount of gases (Andrawes et al., 1984; Graney and Kesler, 1995). However, it is noteworthy that the amounts of gases generated are negligible when the crushing is buffered by mineral grains (Blamey, 2012). The pestle drop numbers (expressed as "drops" in the following text) of each crushing step (one step represents one extraction) were carefully arranged to maintain volatile concentrations at high enough level for the measurements. Gases released from each extraction were introduced into the quadruple immediately and then analyzed by the QMS using the Faraday cup in a static mode. During the measurement, the electron emission current was set at 0.01 mA to reduce the ionization efficiency in order to avoid saturation of high concentration species. The QMS was operated in rapid scan mode with a mass range of 1–65 amu. As such, the interferences due to conversion of one gas species to another, such as CO_2 to CO, by hot filaments, if any, are maintained at a very low level. The electron energy (equal to the voltage difference between the filament and anode grid) during the measurements was maintained at 70 eV and the ion energy (equal to the voltage biasing of the anode grid) at the highest setting, i.e., 12 eV, which can increase the throughput and the sensitivity of the mass spectrometer. The absolute resolution ($\Delta M_{10\%}$), which is defined as the peak width where the signal decreases to 10% of the maximum value, is 0.5 amu. The experiment terminated when the signals of the investigated major gas species fall to background level. As a result, sample material was generally crushed several to ten thousands of drops and was mostly powdered to 1–4 μm in size (Bai et al., 2013), leading to the breakup of most fluid inclusions (>4 μm, Fig. 2). Gas species were identified according to their standard fragmentation patterns from the RGA (Residual Gas Analyzer) software library. When several gas species have overlapping peak patterns, their strongest peaks with the least interferences from other gas fragments were chosen for quantification. In this case, fragmentation patterns stored in the RGA software library were used for conversion. Major gas species identified in this study and their corresponding peak values used are listed below: CO_2 (44 amu), CH_4 (16 amu), H_2O (18 amu), N_2 (14 amu), formamide (CH_3NO, 45 amu), C_2H_6 (30 amu), C_3H_8 (29 amu), C_4H_{10} (43 amu), C_2H_2 (25 amu), O_2 (32 amu), He (4 amu) and Ar (40 amu). With these standard fragmentation patterns, qualitative and moderately quantitative determination of gas species from each step is possible.

4. RESULTS

4.1. Raman spectroscopy

The Raman spectroscopic analyses were only applied to semi-transparent cassiterite and transparent quartz minerals and not on the opaque wolframite mineral. The compositional characteristics of the primary (PFIs) and secondary (SFIs) fluid inclusions within the studied minerals are shown in Figs. A2–A3, Appendix A and Fig. 3. A sketch map of the fluid inclusion within the minerals is shown in Fig. 3a and calculated relative Raman peak areas of CO_2 and CH_4 (expressed as $A(CO_2/CH_4)$) of different fluid inclusion groups are summarized in Fig. 3b and Table B1, Appendix B. As the Raman peak areas of different gas species are proportional to the molecule numbers of the respective species in the vapors (Seitz et al., 1996), the relative peak areas of gases should be proportional to their molar ratios. The estimated proportions of different types of fluid inclusions in each studied mineral are listed in Table 1.

4.1.1. Fluid inclusions within wolframite and cassiterite

Fluid inclusions in the wolframite sample 13YGX06Wlf are mainly large-sized, irregular aqueous bi-phase SFIs (generally > 20 μm) and small-sized aqueous bi-phase PFIs (generally < 10 μm). Minor gas-rich fluid inclusions are locally present within the sample (Fig. 2b). There are also some very fine SFIs (<5 μm) distributed as trails or clusters (Fig. 2b).

Fluid inclusions in the cassiterite sample 13YGX36Cst are dominated by isolated aqueous bi-phase PFIs in regular to negative crystal shapes associated with subordinate

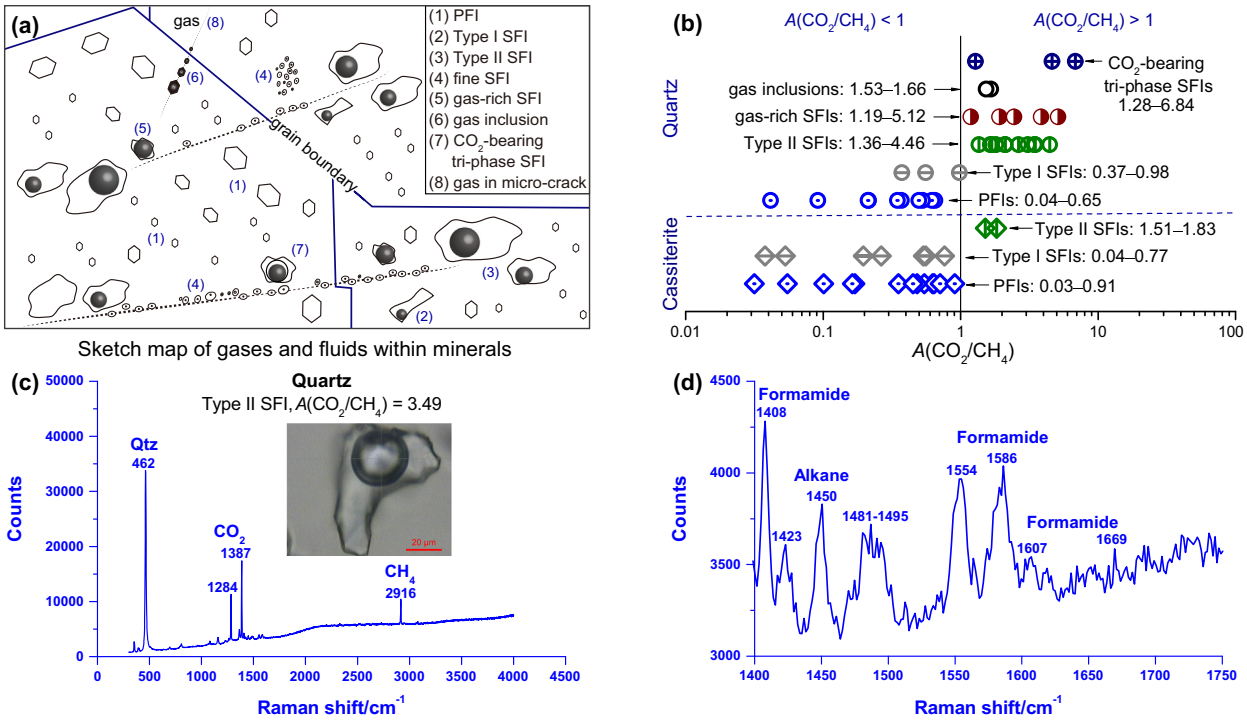

Fig. 3. Sketch map showing the occurrence of fluid inclusions in different forms (a) and Raman results (b–d). (b) Calculated Raman $A(CO_2/CH_4)$ values of fluid inclusions within cassiterite and quartz samples. The relative peak areas of CO_2 and CH_4 (expressed as $A(CO_2/CH_4)$) were calculated by area ratios of Raman peaks for CO_2 and CH_4. (c–d) Raman spectra and photomicrograph of Type II secondary fluid inclusion. PFI and SFI represent primary and secondary fluid inclusion, respectively. In figure (d), small Raman peaks at 1430–1390 cm^{-1}, 1620–1585 cm^{-1} and 1669 cm^{-1} can be assigned as N—H (amide III band) stretching, C—N (amide II band) vibration and C=O stretching vibration of primary amide, respectively (Lees et al., 1981; Ke, 1998; Frost et al., 2001). The Raman peak at 1607 cm^{-1} can be ascribed to formamide dissolving in water, according to the experimental result of Puranik and Ramiah (1959). Besides, the Raman peak at 1450 cm^{-1} is mostly attributed to the CH_2 wagging mode of straight chain alkanes (e.g., Pironon et al., 1995).

Table 1
Fluid inclusion types and proportions in minerals.

Mineral samples	Types	PFI	Type I SFI	Type II SFI	Fine SFI	Gas-rich SFI	Gas inclusions	Other types
	Phases	Bi-phase				Bi-phase	Single phase	
	Description	Liquid-rich				Gas-rich	Gas vapor	
Sample 13YGX06, mineral association: quartz, muscovite, wolframite, pyrite, chalcopyrite, arsenopyrite, cassiterite								
13YGX06Wlf	Proportions	~40%	~50%		~6%	~3%	~1%	–
	Diameter	<10 μm	20–100 μm		<5 μm	<10 μm	<10 μm	
Sample 13YGX36, mineral association: quartz, muscovite, K-feldspar, cassiterite, pyrite, fluorite, arsenopyrite, wolframite								
13YGX36Cst	Proportions	~40%	~35%	~15%	<4%	<1%	<1%	~4%
	Diameter	<100 μm	20–150 μm	~20 μm	<5 μm	~15 μm	~15 μm	
13YGX36Qtz	Proportions	~36%	~3%	~43%	~4%	~5%	~4%	<5%
	Diameter	<20 μm	~20 μm	15–80 μm	<5 μm	15–60 μm	10–40 μm	

Note: the fluid inclusion proportions were visually estimated. Symbol "–" denotes insignificant amounts or absent. PFI and SFI represent primary and secondary fluid inclusion, respectively.

large, elongated and irregular-shaped aqueous bi-phase Type I SFIs distributed linearly or along micro-cracks (Fig. 2c and d). In both types, the gas mixtures are dominated by CH_4 with low $A(CO_2/CH_4)$ values (lower than 1, Figs. 3b and A2). Raman spectra of the PFIs indicate that the mineralizing fluids associated with the formation of the cassiterite are rich in CH_4. In addition, some Type II SFIs with higher vapor/liquid ratios (Fig. 2e) and $A(CO_2/CH_4)$ values (higher than 1, Fig. 3b) relative to the PFIs are distributed along micro-cracks. Some fine SFIs in clusters (<5 μm, Fig. 2d) are too small to be analyzed.

4.1.2. Fluid inclusions within vein quartz

Fluid inclusions in the vein quartz sample 13YGX36Qtz are different from those in ore minerals, in terms of the types of fluid inclusions and their respective volume

proportions (Table 1). PFIs in the vein quartz are aqueous bi-phase, small and generally have negative crystal shapes. Besides H_2O, the gases in the vapor phase are dominated by CH_4 with minor or non-detectable CO_2, which results in very low $A(CO_2/CH_4)$ values (<1, Fig. 3b). Raman spectra of PFIs in quartz suggest that the fluids associated with the formation of the vein quartz are $CH_4 + H_2O$ fluids with insignificant CO_2 contents.

Several types of aqueous bi-phase SFIs are also identified in this sample: CH_4-rich Type I SFIs and CO_2-rich Type II SFIs. Type I SFIs are sporadic and generally have elongated shapes with sharp re-entrants. This type of SFIs is characterized by lower $A(CO_2/CH_4)$ ratios (<1) relative to Type II SFIs (Figs. 3b and A3). Type II SFIs are the dominant SFI type in quartz. They have large volumes and irregular shapes and generally distribute along micro-cracks or healed micro-fissures (Fig. 2f and g). The volatiles in these SFIs mainly consist of CO_2 and CH_4 with very high $A(CO_2/CH_4)$ values (1.36–4.46, Fig. 3b). In addition to CH_4–CO_2–N_2 mixtures, Raman microprobe has also detected minor straight chain alkanes together with formamide in big Type II SFIs with large vapors (Fig. 3c and d), which correspond to a later CO_2-rich and organic matter bearing hydrothermal fluid. Some fine SFIs distributed along micro-cracks (Fig. 2g) are too small to be analyzed.

Minor gas inclusions and gas-rich secondary fluid inclusions also appear in the quartz sample. They are generally linearly distributed along healed or unhealed micro-cracks (Fig. 2h). These inclusions are composed essentially of CO_2 and CH_4 with relatively high $A(CO_2/CH_4)$ ratios (>1, Fig. 3b). A few CO_2-bearing tri-phase fluid inclusions are also identified in the quartz sample, with $A(CO_2/CH_4)$ ratios > 1 (Fig. 3b).

4.2. Carbon isotopic composition

Stable carbon isotope analyses were carried out on five vein quartz samples and the results are presented in Table B2, Appendix B. The analyses yielded almost uniform $\delta^{13}C$-CH_4 values ranging from −41.7‰ to −39.4‰ and relatively consistent $\delta^{13}C$-CO_2 values ranging from −7.22‰ and −6.14‰.

4.3. QMS gas analyses of unirradiated minerals

Unirradiated wolframite sample 13YGX06Wlf, cassiterite sample 13YGX36Cst and vein quartz sample 13YGX36Qtz were selected for fluid inclusion QMS gas analyses. The compositions of the gases released from the fluid inclusions are presented in Table B3, Appendix B.

Volatile constituents of the fluid inclusions within the studied minerals mainly consist of CO_2, CH_4, N_2, H_2O, formamide, some other light hydrocarbons as well as minor He, Ar, and O_2. Although the compositions of these components vary from one crushing step to another (Table B3), gases extracted from the initial crushing stage (usually less than tens to hundreds of drops) and the final crushing stage (usually after hundreds of drops) show obvious compositional differences, such as distinct CO_2/CH_4 ratios (Fig. 4a–c), different CO_2, CH_4 and N_2 concentrations (Fig. 4d–f) as well as light hydrocarbon compositions (Fig. 4g–i). In general, gases released in the initial crushing stage are CO_2-rich with high CO_2/CH_4 ratios (>1), whereas gases liberated in the final crushing stage are dominated by CH_4 with low CO_2/CH_4 ratios (<1) with distinct C_3H_8 and C_4H_{10} contents relative to the initial crushing stage (see Fig. 4). Based on the compositional variations of the extracted gases, an intermediate stage could also be distinguished, which appears to result from mixtures of gases released during the initial and the final crushing stages (Fig. 4).

4.4. $^{40}Ar/^{39}Ar$ geochronology *of irradiated minerals*

Muscovite sample 13YGX36Ms and K-feldspar sample 13YGX36Kfs were chosen for $^{40}Ar/^{39}Ar$ dating by stepwise heating (see Fig. 5). The corresponding wolframite, cassiterite and vein quartz samples that were selected for QMS gas analyses were also analyzed for fluid inclusion $^{40}Ar/^{39}Ar$ stepwise crushing (see Figs. 6 and 7). The $^{40}Ar/^{39}Ar$ results are summarized in Tables B4–B6, Appendix B.

4.4.1. Muscovite and K-feldspar stepwise heating experiment

Stepwise heating of the muscovite sample 13YGX36Ms yielded flat age spectrum with a plateau age of 156.2 ± 0.9 Ma (MSWD = 0.5) (Fig. 5a), which is consistent with the timing of tungsten mineralization as discussed in Section 2.1. The K-feldspar 13YGX36Kfs heating experiment formed a saddle-shaped age spectrum with apparent ages ranging from 498 to 96.0 Ma (Fig. 5b). The last several steps defined an inverse isochron with an age of 129.2 ± 3.1 Ma (MSWD = 5.5) (Fig. 5c). The corresponding initial $^{40}Ar/^{36}Ar$ ratio of 361.9 ± 26.0 suggests excess argon interference. After excluding excess ^{40}Ar with the initial $^{40}Ar/^{36}Ar$ value (361.9), the last several steps yielded a concordant plateau age of 129.2 ± 2.1 Ma (MSWD = 4.7) (Fig. 5b). We interpret this K-feldspar $^{40}Ar/^{39}Ar$ age as the timing of a later episode of hydrothermal activity.

4.4.2. Wolframite, cassiterite and vein quartz stepwise crushing experiment

Stepwise crushing experiments of wolframite, cassiterite and vein quartz samples yielded similar decreasing $^{40}Ar/^{39}Ar$ age spectra for the first several steps, which are characterized by a quick decline with abnormally old apparent ages. In contrast, for the final steps, the wolframite sample 13YGX06Wlf and the vein quartz sample 13YGX36Qtz formed increasing age spectra with older apparent ages, whereas the cassiterite sample 13YGX36Cst yielded a flat age spectrum defining a precise plateau age. The final steps of each experiment formed well-defined inverse isochrons.

The isochron of the wolframite sample 13YGX06Wlf (steps 5–24, 10,600 drops of crushing, 10,730 drops in total, Fig. 6b) has an initial $^{40}Ar/^{36}Ar$ ratio of 322.4 ± 1.3 higher than the atmospheric ratio of 295.5 (Steiger and Jäger, 1977), which implies excess argon disturbance. Excluding excess ^{40}Ar with the initial $^{40}Ar/^{36}Ar$ value (322.4) yields a flat age spectrum with a plateau age of 159.3 ± 1.9 Ma (MSWD = 0.4) (Fig. 6a), which is consistent with the

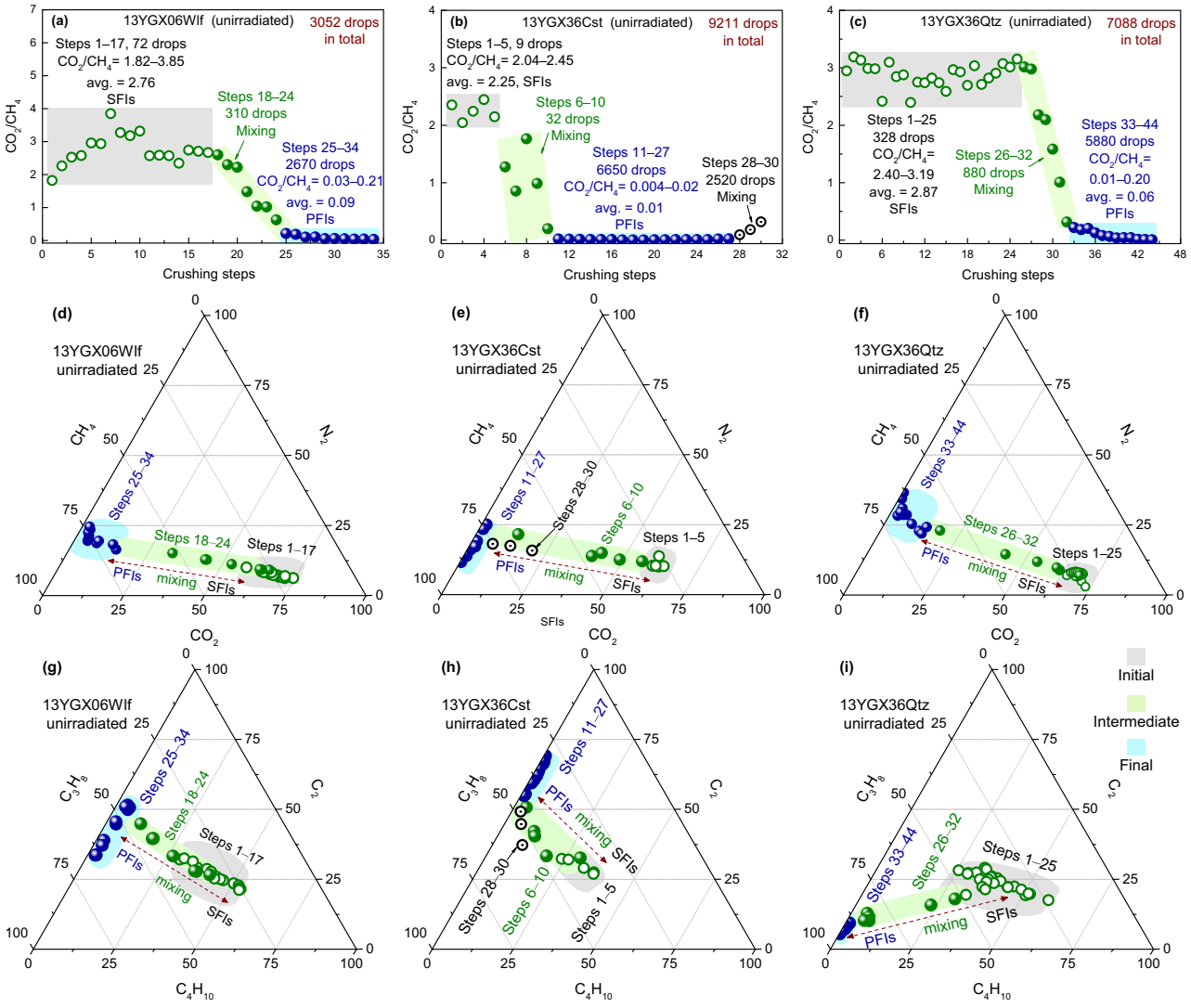

Fig. 4. QMS gas compositional variations during stepwise crushing of the unirradiated minerals. (a–c) CO_2/CH_4 ratios. (d–f) CH_4–N_2–CO_2 ternary diagrams. (g–i) C_2–C_3H_8–C_4H_{10} ternary diagrams, C_2 includes C_2H_6 and C_2H_2. "Initial", "Intermediate" and "Final" in the legends represent different crushing stages and are labeled by shadows. One crushing step represents one extraction. The pestle drop numbers (referred to as "drops") of each crushing stage are presented in figure a–c. PFI and SFI represent primary and secondary fluid inclusion, respectively. "Mixing" represents mixed gases between primary and secondary fluid inclusions.

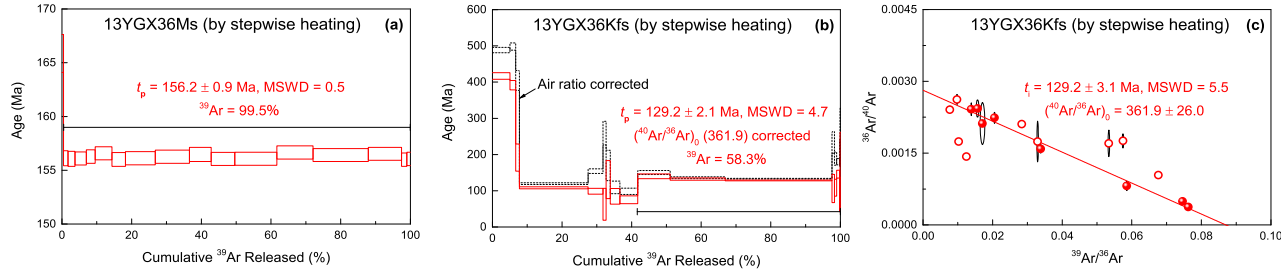

Fig. 5. Stepwise heating $^{40}Ar/^{39}Ar$ results of muscovite and K-feldspar. The plateau ages (solid red lines) of the muscovite sample 13YGX36Ms and the K-feldspar sample 13YGX36Kfs were calculated by assuming trapped initial $^{40}Ar/^{36}Ar$ ratios of 295.5 and 361.9, respectively. The black dotted line in figure b is an air ratio (295.5) corrected age spectrum. Error ellipses are presented with black ellipses in the inverse diagram.

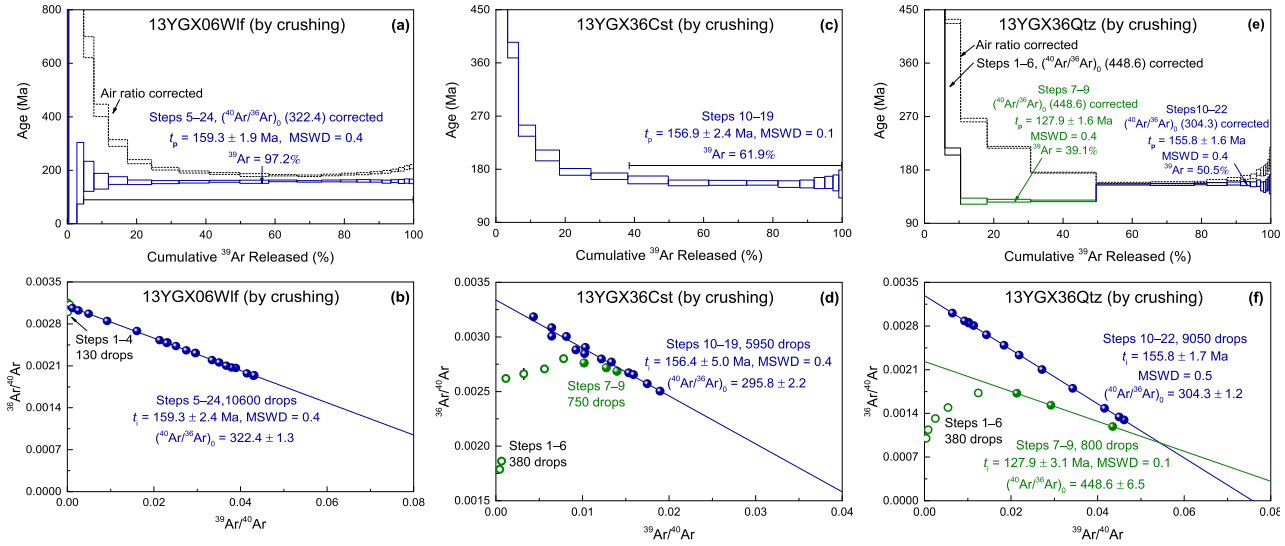

Fig. 6. Fluid inclusion ^{40}Ar/^{39}Ar results of wolframite, cassiterite and vein quartz from the Yaogangxian tungsten deposit. The plateau ages (solid blue lines) were calculated by assuming trapped initial ^{40}Ar/^{36}Ar ratios of 322.4, 295.5 and 304.3, respectively. The plateau age (solid green line) of the quartz sample 13YGX36Qtz was calculated with a trapped initial ^{40}Ar/^{36}Ar ratio of 448.6. The black dotted lines in a&e are air ratio (295.5) corrected age spectra. The pestle drop numbers and error ellipses are presented in the inverse isochron diagrams. (For interpretation of the references to colour in this figure legend, the reader is referred to the web version of this article.)

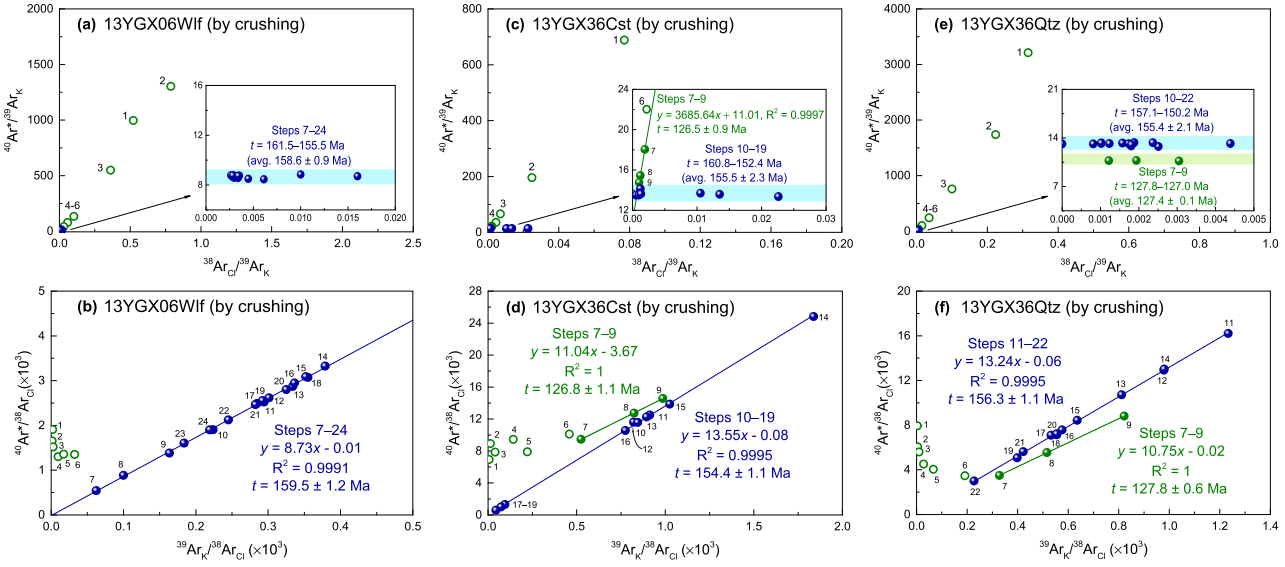

Fig. 7. Correlation diagrams of $^{38}Ar_{Cl}$, $^{39}Ar_K$, and $^{40}Ar^*$ (air corrected radiogenic argon) of irradiated wolframite, cassiterite and vein quartz from the Yaogangxain tungsten deposit. $^{38}Ar_{Cl}$, $^{39}Ar_K$ were produced by neutron-induced reactions from Cl, and K, respectively. The ages of the final steps of all these samples and steps 7–9 of the quartz sample 13YGX36Qtz were calculated using the initial ^{40}Ar/^{36}Ar ratios (322.4, 295.8, 304.3, and 448.6, respectively), and the other steps were calculated using the atmospheric ratio (295.5) to exclude non-radiogenic argon. Step 10 of the quartz sample 13YGX36Qtz has not been shown in Fig. 7f due to the low $^{38}Ar_{Cl}$ signal of 0.

isochron age of 159.3 ± 2.4 Ma (MSWD = 0.4) for this sample.

The cassiterite sample 13YGX36Cst formed a flat age spectrum with the last 10 steps (steps 10–19, crushed 5950 drops, 7080 drops in total, Fig. 6c) yielding a plateau age of 156.9 ± 2.4 Ma (MSWD = 0.1). This age is accordant with its inverse isochron age of 156.4 ± 5.0 Ma (MSWD = 0.4) with an initial ^{40}Ar/^{36}Ar ratio of 295.8 ± 2.2 (Fig. 6d) that agrees well with the atmospheric ^{40}Ar/^{36}Ar ratio (295.5).

The crushing experiment of the vein quartz sample 13YGX36Qtz defined two isochrons (Fig. 6f). The last 13 steps (steps 10–22, 9050 drops of crushing, 10,230 drops in total) accounting for 50.5% of total released ^{39}Ar yield an isochron age of 155.8 ± 1.7 Ma (MSWD = 0.5) with an initial ^{40}Ar/^{36}Ar value of 304.3 ± 1.2 that is slightly

higher than the modern atmospheric $^{40}Ar/^{36}Ar$ value. Excluding excess ^{40}Ar with the initial $^{40}Ar/^{36}Ar$ value (304.3) yields a plateau age of 155.8 ± 1.6 Ma (MSWD = 0.4) (Fig. 6e). On the other hand, steps 7–9 (crushed 800 drops) with 39.1% total ^{39}Ar released form an additional well-defined isochron with an age of 127.9 ± 3.1 Ma (MSWD = 0.1), which corresponds to a plateau age of 127.9 ± 1.6 Ma (MSWD = 0.4) when excess ^{40}Ar is excluded with the initial $^{40}Ar/^{36}Ar$ ratio (448.6) (Fig. 6e).

4.4.3. Correlations between Cl- and K-derived argon isotopes

Gases released during the first several crushing steps are usually characterized by high $^{40}Ar^*$ and $^{38}Ar_{Cl}$ but negligible $^{39}Ar_K$ concentrations (Table B6), resulting in high $^{40}Ar^*/^{39}Ar_K$ and $^{38}Ar_{Cl}/^{39}Ar_K$ ratios in the correlation diagrams of $^{38}Ar_{Cl}$, $^{39}Ar_K$, and $^{40}Ar^*$ (see Fig. 7). After several hundred rounds of crushing, the experiment of cassiterite sample 13YGX36Cst exhibits good linear correlations on plots of Cl–K–Ar^* correlations during steps 7–9, the Y-intercept in Fig. 7c and the slope in Fig. 7d correspond to an age of *ca.* 127 Ma. Likewise, crushing steps 7–9 of the vein quartz sample 13YGX36Qtz have nearly constant $^{40}Ar^*/^{39}Ar_K$ ratios, corresponding to accordant apparent ages of 128–127 Ma (Fig. 7e). They also form a correlation line on the plot of $^{40}Ar^*/^{38}Ar_{Cl}$ versus $^{39}Ar_K/^{38}Ar_{Cl}$, with an apparent age of 128 Ma calculated from the slope (Fig. 7f). These ages are consistent with its corresponding inverse isochron and plateau ages mentioned above (Fig. 6e and f).

As the crushing experiment proceeds, the $^{40}Ar^*/^{39}Ar_K$ ratios dropped to relatively uniform levels and the $^{39}Ar_K/^{38}Ar_{Cl}$ ratios varied significantly due to the extremely low $^{38}Ar_{Cl}$ signals (Fig. 7b, d&f, Table B6). These lower and constant $^{40}Ar^*/^{39}Ar_K$ ratios correspond to constant apparent ages, showing good linear correlations on plots of $^{40}Ar^*/^{38}Ar_{Cl}$ versus $^{39}Ar_K/^{38}Ar_{Cl}$. The ages calculated from average $^{40}Ar^*/^{39}Ar_K$ ratios (Fig. 7a, c&e) as well as those from the slopes of the regression lines (Fig. 7b, d&f) agree well with their respective plateau and isochron ages calculated using traditional methods as discussed above (see Fig. 6).

5. DISCUSSION

5.1. Towards a better understanding of gas release patterns during crushing

Based on QMS gas analyses, the gas release of stepwise crushing can be outlined in three distinctive stages (see Fig. 8a–c): (1) the initial crushing stage is characterized by CO_2-enriched and H_2O-free mixtures with high CO_2/CH_4 ratios > 1; (2) the intermediate crushing stage shows more release of water, ethane, and formamide; and (3) the final crushing stage is marked by the significant output of CH_4 with steeply decreasing output of CO_2, down to an insignificant constituent. Combined with micrographic observations as well as the results of Raman spectroscopic studies, these findings provide direct constraints on the behavior of gas extraction during stepwise crushing, as summarized in the sub-sections below.

5.1.1. Preferential release of vapor-rich SFIs in the initial crushing stage

Regardless of which mineral was crushed, data points of the first several to tens of crushing steps exhibited scattered and high CO_2/CH_4 ratios (larger than 1, Fig. 4a–c) along with insignificant amounts of H_2O (Fig. 8a–c). Based on the results of Raman, the SFIs are commonly CO_2-dominated with high vapor $A(CO_2/CH_4)$ ratios (>1, Fig. 3b). They are different from the PFIs, which have low vapor $A(CO_2/CH_4)$ ratios (<1, Fig. 3b) and are enriched in CH_4. Therefore, the gas mixtures released in these steps are likely significantly derived from the SFIs. Additionally, the low H_2O contents in the initial crushing stage relative to the other ones suggest that these gases should be extracted mainly from gas-rich fluid sources rather than aqueous sources. Therefore, such sources could be vapor-rich SFIs (including gas inclusions and gas-rich secondary fluid inclusions) since they generally distribute along micro-cracks and seem to be easily released without significant buffering effect from the fluid phase. Meanwhile, fluid inclusions that have high vapor/liquid ratios and distribute along micro-cracks, e.g., Type II SFIs (Fig. 2e–g), may be also released in the initial crushing stage. Alternatively, gas mixture trapped in mineral micro-cracks could be preferentially extracted in the first few crushing steps.

5.1.2. Large aqueous SFIs-dominated mixing release

As crushing progresses, the outputs of water, ethane, and formamide begin to rise significantly, which is particularly obvious for the quartz sample (see Fig. 8). Such features may suggest significant gas release from aqueous and organic matter bearing fluid inclusions, specifically, the large, irregular, formamide and alkane bearing Type II SFIs as shown in Figs. 2 and 3. Large PFIs with higher vapor/liquid ratios should also be broken in these steps, which explains the steady decrease in CO_2/CH_4 ratios over time during the crushing experiments (Fig. 4a–c) and the linear mixing relationships observed in triangle diagrams (Fig. 4d–i). Occasionally, SFIs-derived components could become more dominant, when the contribution from PFIs is negligible. In this scenario, the released gases would provide information on the chemistry and geochronology of the SFIs that are otherwise difficult to obtain, as shown by Bai et al. (2018a).

5.1.3. Final liberation of small PFIs in the final crushing stage

The uniform low CO_2/CH_4 ratios (<1, Fig. 4a–c) in the last several crushing steps probably suggest predominant liberation of the smaller CH_4-rich PFIs. Gases released in these steps could therefore bear crucial information of ore-forming processes, during which the PFIs formed.

The cassiterite sample 13YGX36Cst is one exception. For this sample, the final three crushing steps (pestle drop numbers over 6691) released higher proportions of formamide and CO_2 (Fig. 8b). As large molecules, the formamide and CO_2 are preferentially hosted by fluid inclusions rather than mineral lattice and defects. Given the compositional characteristics of the gases released from the last several steps, which more strongly resemble those

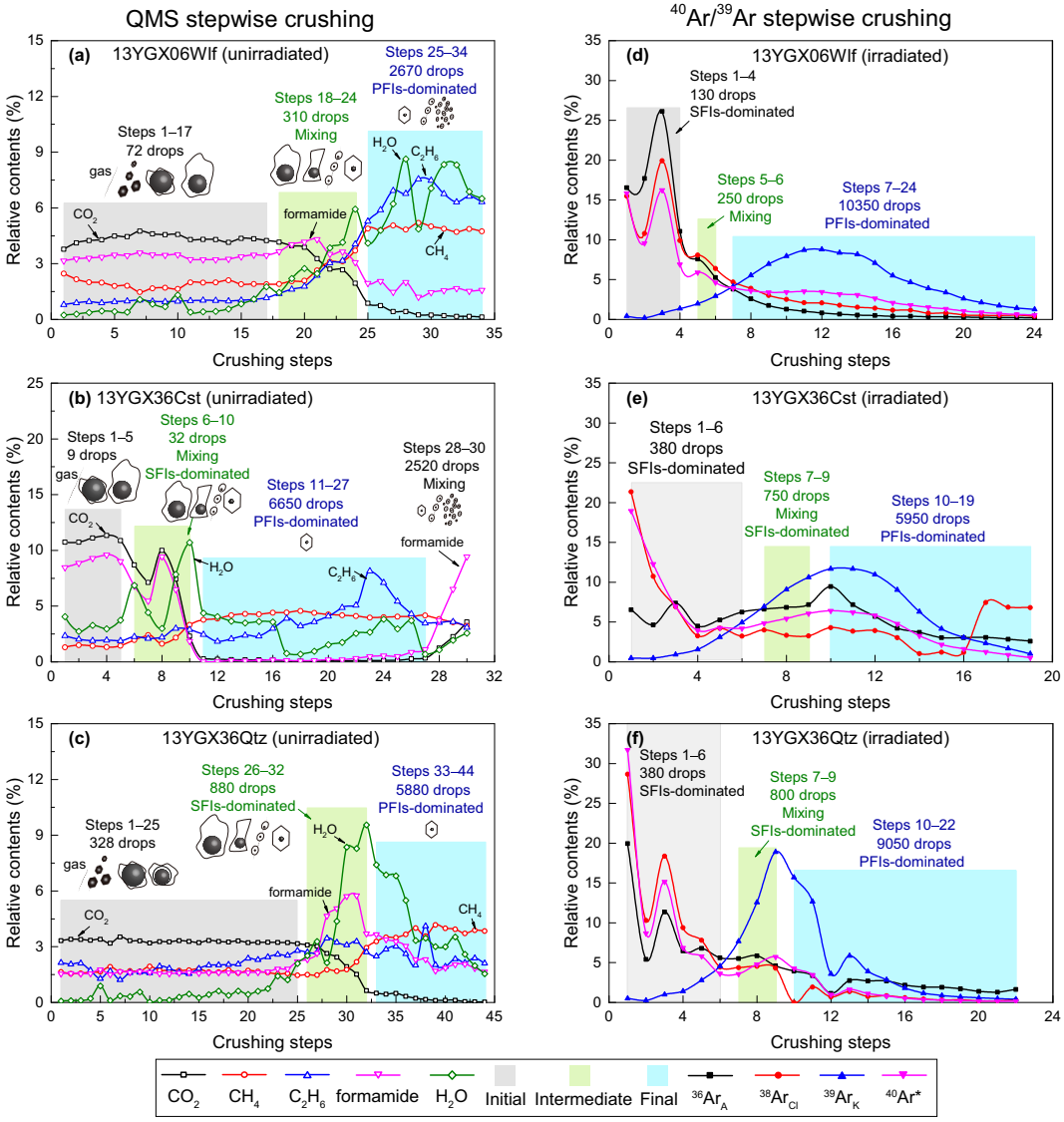

Fig. 8. Compositional characteristics of major gas components released by QMS stepwise crushing (a–c) and of argon isotopes released by ^{40}Ar/^{39}Ar stepwise crushing (d–f). The relative proportion (r) represents the content of each crushing step (C_i) accounts for the proportion of the total contents of all the crushing steps ($\sum_{i=1}^{n} C_i$) of gas i, for example, $r = C_i / \sum_{i=1}^{n} C_i$. The content of each gas constitute is presented in Table B3, Appendix B. The pestle drop numbers of each crushing stage are presented and the potential sources are indicated. The expression of different crushing stages and SFI and PFI is the same as Fig. 4.

from the SFIs, we suggest that these gases likely originated from the very fine SFIs that occur as clusters (Fig. 2d).

5.2. Towards a better understanding of fluid inclusion ^{40}Ar/^{39}Ar data

As shown in our stepwise crushing experiments and many previous ^{40}Ar/^{39}Ar crushing experiments, gases released during the first several steps have abnormally high $^{40}Ar^{*}$, $^{38}Ar_{Cl}$, and extremely low $^{39}Ar_{K}$, which lead to decreasing age spectra with unreasonably old apparent ages (e.g., Kelley et al., 1986; Turner and Wang, 1992; Jiang et al., 2012), whereas gases released in the final crushing stage usually show uniform $^{40}Ar^{*}/^{39}Ar_{K}$ ratios with relatively flat age spectra (Qiu and Wijbrans, 2006; Qiu and Jiang, 2007; Qiu and Wijbrans, 2008; Jiang et al., 2012; Bai et al., 2013; Bai et al., 2018a). Sometimes, gases released in the initial or intermediate crushing stage form well-defined isochrons with geologically meaningful ^{40}Ar/^{39}Ar ages (Qiu and Jiang, 2007; Bai et al., 2013). Combined with Raman spectroscopy and carbon isotope results, these phenomena can be explained by the gas release patterns established above.

5.2.1. Fluid origins of secondary and primary fluid inclusions

δ^{13}C isotopic ratios of CH_4-CO_2-bearing geofluids have been widely applied to trace the sources of gases as well as their migration pathways and alteration processes (Morishita, 1991; Lüders et al., 2012; Potter et al., 2013; Lüders and Plessen, 2015). In this study, the measured δ^{13}C values of CH_4 (δ^{13}C-CH_4) vary from −41.7‰ to −39.4‰. Such values are distinct from the δ^{13}C values of

biologically-produced methane (≤−50‰; Schoell, 1988; Whiticar, 1999) and mantle-derived methane (>−25‰, Jenden et al., 1993). The δ^{13}C-CH_4 values of the studied quartz samples are also significantly lower than those originated from sediment-starved hydrothermal systems, which usually range from −20‰ to −5‰ (McCollom, 2008 and references therein). Instead, the measured δ^{13}C-CH_4 values are more similar to those of sediment-related hydrothermal systems which generally have δ^{13}C-CH_4 values between −100‰ and −40‰ (Hinrichs et al., 2006). High-temperature synthesis reactions in fluid-rock interaction experiments also yield CH_4 with similar δ^{13}C values ranging from −53.6‰ to −19.1‰ (Horita and Berndt, 1999; Taran et al., 2007). Based on the Raman spectra, the PFIs are CH_4-rich, whereas the SFIs are mostly CO_2-rich. As the PFIs are the main source of CH_4, we suggest that they could have formed during fluid-rock interaction processes. Indeed, in CO_2/CH_4 versus N_2/Ar space, gases from the final crushing stage, which represent PFIs-derived gas mixtures (as discussed in Section 5.1.3), scatter in the fields between evolved magmatic fluids and organic crustal water (meteoric fluids equilibrated with crustal rocks and contaminated by organic matters, N_2, He and hydrogen sulfide from wall rocks, Norman and Moore, 1999) (Fig. 9). This observation further supports the hypothesis that fluid-wall rock interaction contributes to the mineralization process in the investigated deposit, in other word, the W-Sn-bearing magmatic-hydrothermal fluids interacted with the metasedimentary wall rocks which promoted mineral precipitation (e.g., Lecumberrisanchez et al., 2017).

δ^{13}C compositions of CO_2 (δ^{13}C-CO_2 = −7.22‰ to −6.14‰) of analyzed samples, on the other hand, are indistinguishable from those of mantle-derived carbon (−8‰ to −5‰; Deines et al., 1973; Allard, 1982; Hoefs, 2009) and magmatic carbon (about −9‰ to −4‰, Blank et al., 1993). However, they are distinct from those of marine carbonate (−2‰ to +1‰, Hoefs, 2009) and organic carbon (−25‰ to −20‰, Kawagucci et al., 2013). This may indicate a deep-seated source, such as mantle-derived or magmatic-originated, for the CO_2-dominated fluid inclusions, i.e., SFIs. This hypothesis is further supported by the observation that gases from the initial crushing stage, which represent SFIs-derived gas mixtures (as discussed in Section 5.1.1), plot close to the field of magmatic waters in CO_2/CH_4 versus N_2/Ar space (Fig. 9).

5.2.2. Excess argon and high chlorine in the first crushing steps

As discussed above, the CO_2-rich fluids, such as the SFIs, likely have a deep-seated origin. Geofluids originated from deep-seated sources generally contain significant amounts of excess argon ($^{40}Ar_E$) with abnormally high ^{40}-Ar/^{36}Ar ratios (Ozima and Podosek, 1983; Ozima et al., 1989; Turner and Wang, 1992; Qiu and Wijbrans, 2006; Kendrick et al., 2011). For example, the shallow MORB mantle has ^{40}Ar/^{36}Ar ratios up to 28,000 (Niedermann and Bach, 1998). Crustal fluids trapped in the oldest known alunite (1.87 Ga) have ^{40}Ar/^{36}Ar ratios of 584–629 (Landis et al., 2005). Deep-seated fluids trapped within minerals of lower crustal granulites from the Belomorian Mobile Belt have ^{40}Ar/^{36}Ar ratios of 393–2350 (Vetrin et al., 2007). These values are significantly higher than the atmospheric value. Gases released in the initial crushing stages of the studied mineral samples typically show high $^{40}Ar^*$ signals (Fig. 8d–f) with high ^{40}Ar/^{36}Ar ratios ranging from 317.1 to 999.8 (Table B5), which indicate the presence of $^{40}Ar_E$ in the fluid inclusions.

In addition to high $^{40}Ar_E$ concentrations, gases released during the first few crushing steps are also characterized by very high Cl (represented by $^{38}Ar_{Cl}$) concentrations (Fig. 8d–f) with linear correlations between $^{40}Ar^*$ and $^{38}Ar_{Cl}$ (Fig. 7a, c&e). The Cl–K–Ar^* correlations were thoroughly discussed in early ^{40}Ar/^{39}Ar studies (Kelley et al., 1986; Turner and Bannon, 1992; Turner and Wang, 1992). These studies all found clear linear correlations between Cl and $^{40}Ar_E$. The potential source of these $^{40}Ar_E$ and Cl-derived ^{38}Ar was suggested as gases dissolved in the inclusion brines (Turner and Bannon, 1992). Stepwise crushing experiments of Jiang et al. (2012) showed a good correlation between $^{40}Ar^*$ and $^{38}Ar_{Cl}$ for the SFIs-originated gases.

Combined analyses of QMS gas composition and ^{40}Ar/^{39}Ar geochronology in this study led to a new understanding of the sources of the highly correlated $^{38}Ar_{Cl}$ and $^{40}Ar_E$ in the initial crushing stage as summarized below. The results of QMS stepwise crushing experiments show that the gases released in the initial crushing stage

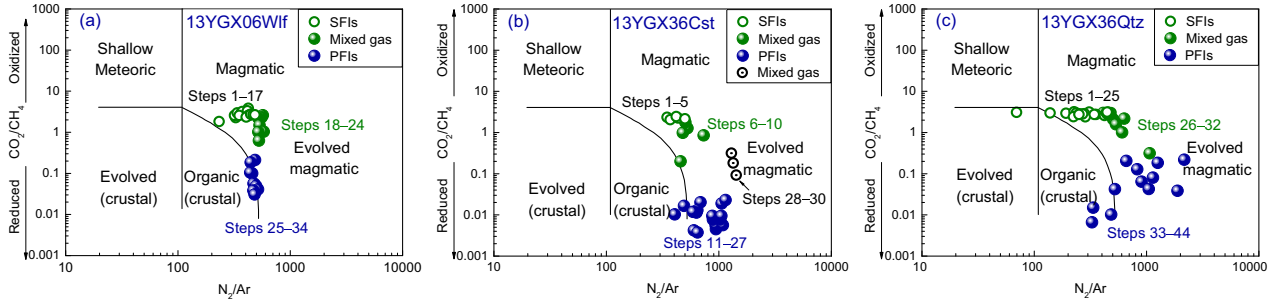

Fig. 9. Plots of CO_2/CH_4 versus N_2/Ar ratios of the studied samples. The diagram is developed by Norman and Moore (1999) and improved by Blamey (2012) to distinguish fluid origins, i.e., magmatic, evolved magmatic, shallow meteoric and crustal sources. Evolved crustal fluids represent meteoric fluids approximately in equilibrium with crustal rocks or gases such as organic species derived from the wall rock. Contamination of high nitrogen-bearing basinal fluids can elevate N_2/Ar ratios into an "organic crustal fluid field". Evolved magmatic fluids represent composite fluids consist of various proportions of volatiles from magmatic, crustal, and/or meteoric sources.

are CO_2-dominated and H_2O-free (Fig. 8a–c). This observation supports the hypothesis that gases extracted from the initial crushing stage mainly come from large-sized vapor-rich SFIs and micro-cracks. Similar to CO_2, Cl is also an important volatile in magmatic systems (Lowenstern, 1995; Naumov et al., 2008; Melluso et al., 2012). Fluids with excess argon, Cl (HCl or Cl_2), and CO_2 from deep degassing processes could be trapped in mineral micro-cracks and form SFIs. Considering the low fluid salinities in the investigated deposit (Li et al., 2017), dissolved Cl in the liquid phases of the SFIs is unlikely to reach high concentrations. Therefore, gas vapors in fluid inclusions should be the most important reservoir for Cl and $^{40}Ar_E$. Additionally, vapor-rich SFIs would naturally be more enriched in Cl and $^{40}Ar_E$ than the liquid-rich ones. On the other hand, dissolved K is also unlikely to reach high concentrations in the low-salinity fluid, and limited liquid phases in the vapor-rich fluid inclusions would therefore result in lower concentrations of K. As a result, the preferential breakage of SFIs, especially the vapor-rich SFIs in the initial crushing stage, should give rise to high and correlated $^{40}Ar_E$ and $^{38}Ar_{Cl}$, but very low $^{39}Ar_K$ signals. This explains the abnormally old apparent $^{40}Ar/^{39}Ar$ ages and nearly consistent $^{40}Ar_E/^{38}Ar_{Cl}$ ratios that are often obtained from the initial crushing stage (Figs. 6 and 7).

5.2.3. Post-mineralization hydrothermal events recorded by aqueous SFIs

Integrated micrographic observations, Raman spectroscopic study, and QMS analyses suggest that gases derived from the large aqueous SFIs may dominate the gas mixtures released during the intermediate crushing stage (as discussed in Section 5.1.2). As such, potentially meaningful age measurements for the SFIs could be achieved by $^{40}Ar/^{39}Ar$ analyses during these crushing steps.

The $^{40}Ar/^{39}Ar$ crushing experiment of the vein quartz sample 13YGX36Qtz yielded consistent *ca.* 128 Ma plateau and isochron ages (Fig. 6e and f) as well as ages inferred from Cl–K–Ar^* correlations (Fig. 7e and f) for crushing steps 7–9 (800 drops of the total 10,230 drops). The coexisting cassiterite 13YGX36Cst also yielded similar ages of *ca.* 127 Ma for crushing steps 7–9 (750 drops of the total 7080 drops) on Cl–K–Ar^* correlation diagrams (Fig. 7c and d). These ages agree with the age of the late K-feldspar vein 13YGX36Kfs (129.2 ± 2.1 Ma, Fig. 5b) dated by $^{40}Ar/^{39}Ar$ stepwise heating. This coincidence suggests a genetic link between the formation of SFIs and the development of K-feldspar vein in the quartz vein sample 13YGX36. Given that the late K-feldspar veins crosscut the ore-bearing quartz veins (e.g., Fig. 2a), the ages of 129–127 Ma can be considered as the timing of a major hydrothermal disturbance that is responsible for the formation of SFIs and the generation of the K-feldspar veins. This result is corroborated by findings of Bai et al. (2018a), who reported similar $^{40}Ar/^{39}Ar$ ages for the SFIs and a young K-feldspar vein from the Piaotang tungsten deposit located ~100 km to the east of the studied deposit (Fig. 1a).

The QMS stepwise crushing experiments further support the hypothesis that the $^{40}Ar/^{39}Ar$ ages of 128–127 Ma of the cassiterite and quartz samples should be associated with the SFIs. The significantly higher proportions of H_2O, formamide, and ethane in the gases released during the intermediate crushing stages of these minerals (Fig. 8a–c), especially for the quartz sample 13YGX36Qtz, indicate that significant amounts of gases were released from Type II SFIs, which are large, liquid-rich and contain formamide and alkane. As the Type II SFIs prevail in the quartz sample, their extensive gas release would be able to provide sufficient potassium-derived argon to form the observed additional isochron with meaningful $^{40}Ar/^{39}Ar$ age in these steps. For further clarification of this methodology, the readers are referred to the systematical study on isochrons of Bai et al. (2018a), which makes the case that an isochron cannot be obtained if the analyzed gases were a mixture of gases from both PFIs and SFIs, because it is highly unlikely for the progressive crushing technique to release gas mixtures with a constant PFI/SFI proportion for every step.

Gas mixtures can only form isochrons of SFI-derived gases with meaningful age information if K-bearing (liquid-rich) SFIs from the same episode of hydrothermal event dominate some of the sequential steps (e.g., Jiang et al., 2012; Bai et al., 2013). Take the experiment of cassiterite sample 13YGX36Cst as an example. Micrographic observations revealed the development of both large, irregular and liquid-rich Type I and Type II SFIs (Fig. 2d and e, Table 1). The former is dominated by CH_4 in vapors whereas the latter is more enriched in CO_2 (Fig. A2d–f). It is unlikely that they were trapped simultaneously, as the cassiterite sample contains more of Type I SFIs, whereas the quartz sample contains more of Type II SFIs but little to no Type I SFIs. Vein quartz generally has a slightly later formation relative to intergrown tungsten-tin minerals, because it tends to have slightly lower homogenization temperatures than those of tungsten-tin minerals (e.g., Campbell and Panter, 1990; Cao et al., 2009; Dong et al., 2011; Ni et al., 2015). As Type I SFIs prevail in the earlier-formed cassiterite sample but are sporadic in the later-formed vein quartz (see Fig. 2), the formation of Type I SFIs likely corresponds to a hydrothermal/structural event that is simultaneous of or slightly later than the tungsten-tin mineralization. In contrast, Type II SFIs developed in both quartz and cassiterite samples, especially in the later-formed quartz sample (Fig. 2e–g). Therefore, the hydrothermal event that is associated with the formation of the Type II SFIs should postdate tungsten-tin mineralization as well as the formation of Type I SFIs. Type II SFIs could be preferentially extracted during crushing as they generally have larger sizes and higher vapor/liquid ratios relative to Type I SFIs (Fig. 2d and e). Similarly, both types of large and irregular SFIs that distribute along micro-cracks might be preferentially extracted, relative to the smaller and regular PFIs. The QMS crushing experiment of the cassiterite sample (Fig. 8b) revealed a rapid decrease of CO_2 and an increase of H_2O and CH_4 in the intermediate crushing stage, which might indicate degassing of larger Type II SFIs followed by Type I SFIs. These SFI-derived gases did not form an isochron (Fig. 6d) as argon contribution from single-episode SFIs in the related crushing steps were not enough, even though some linear correlations were observed between Cl- and K-derived argon

isotopes (Fig. 7c and d). For the wolframite sample 13YGX06Wlf, a wide range of gas components were released during the intermediate crushing stage (Fig. 8a), which seem to be a mixture of multiple types of fluid inclusions with no dominant source. Therefore, no isochrons (Fig. 6b) or linear correlations (Fig. 7a–b) were observed for these steps.

Similarly, it should be no surprise that neither isochrons (Fig. 6) nor linear correlations on the plots of $^{40}Ar^{*}/^{38}Ar_{Cl}$ versus $^{39}Ar_{K}/^{38}Ar_{Cl}$ (Fig. 7b, d&f) could be obtained for first crushing steps of all the samples because these steps would preferentially release gases from vapor-rich SFIs, which have less liquid phase and lower K contents.

In summary, secondary hydrothermal events can be recorded by the SFIs. However, a significant amount of gases needs to be released from K-bearing aqueous SFIs for $^{40}Ar/^{39}Ar$ dating to yield reasonable age information. This has been shown by a number of previous $^{40}Ar/^{39}Ar$ crushing experiments, which yielded meaningful ages for secondary hydrothermal events (Qiu and Jiang, 2007; Jiang et al., 2012; Bai et al., 2018a).

5.2.4. Dating ore-formation using fluid inclusion $^{40}Ar/^{39}Ar$ geochronology

After the extractions of excess argon-rich gases trapped in the micro-cracks and the SFIs in the initial to intermediate crushing stages, the gas components of small-sized PFIs dominate the extracted gases in the final crushing stage, providing an opportunity to obtain the accurate $^{40}Ar/^{39}Ar$ age of the PFIs, i.e., the ore-forming age.

The final crushing stages of the three studied samples yielded very consistent $^{40}Ar/^{39}Ar$ ages of 159–154 Ma (Figs. 6 and 7). These ages are in agreement with the muscovite $^{40}Ar/^{39}Ar$ stepwise heating result of 156 ± 0.9 Ma (Fig. 5a). More importantly, previous Re–Os dating of molybdenite from similar quartz vein-type samples yielded ages of 161–155 Ma (Peng et al., 2006; Wang et al., 2010) and $^{40}Ar/^{39}Ar$ stepwise heating of hydrothermal phlogopite and muscovite yielded ages of 155–153 Ma (Peng et al., 2006), both of which agree well with the ages obtained for the final crushing stages. These ages also agree well with the crystallization ages of the Yaogangxian composite pluton (158–155 Ma, zircon U–Pb, Li et al., 2011) and fall within the time range of the large-scale granitoid-related tungsten-tin mineralization in Nanling region (Mao et al., 2007; Fu et al., 2013). These observations corroborate our conclusions that the timing of ore-formation can be directly dated by our gentle $^{40}Ar/^{39}Ar$ stepwise crushing experiments, using the techniques described above.

Gases released in the final crushing stages show initial $^{40}Ar/^{36}Ar$ values similar to or slightly higher than that of the atmosphere (Fig. 6b, d&f), especially for the cassiterite sample 13YGX36Cst, which may imply shallow crustal level fluid-rock interaction, a process that is consistent with their methane carbon isotopic results as well as their CO_2/CH_4 and N_2/Ar ratios (Fig. 9). One could argue that excess argon could be released from crustal rocks during fluid-rock interactions, which then becomes trapped in the fluid inclusions leading to high $^{40}Ar/^{36}Ar$ ratios (e.g., Kelley et al., 1986; Turner, 1988; Turner and Bannon, 1992). However, this does not seem to be the case for the PFIs in the investigated deposit. More interestingly, PFIs trapped in ore/gangue minerals from most granite-related W-Sn deposits and skarn-type W-Sn deposits in South China have atmospheric initial $^{40}Ar/^{36}Ar$ ratios (Bai et al., 2013; Wang et al., 2015; Wang et al., 2016). This phenomenon could be due to a shallow depth of ore formation. Granite-related W-Sn depositions in South China, including the one studied here, are generally associated with middle-temperature (around 240–390 °C) and low-salinity (generally less than 10 wt.% NaCl equivalent) mineralizing fluids (Wei et al., 2012; Ni et al., 2015; Li et al., 2017), which correspond to low fluid pressures and shallow depth metallogenesis. On the one hand, the shallow crustal wall rocks could be in equilibrium with meteoric water or meteoric-origin crustal water with atmospheric $^{40}Ar/^{36}Ar$ ratios. On the other hand, the ascending ore-forming fluids could also equilibrate with the atmosphere through regional fault systems. It is noteworthy that crustal gases/fluids with atmospheric $^{40}Ar/^{36}Ar$ ratios in crustal depths of less than 3.5 km are very common worldwide (O'Nions and Ballentine, 1993; Okada et al., 1994).

In any case, the gas release model proposed here should only be used as a reference in gentle stepwise crushing experiments on hydrothermal minerals, as the nature of the fluid inclusions involved could be different. Take the wolframite sample 13YGX06Wlf as an example. Microscopic examination of this sample revealed that very fine SFIs (less than several micrometers) in clusters or tails are prevalent (Fig. 2b). These SFIs could have formed during additional hydrothermal events or stress-induced deformation of the large SFIs, e.g., leakage, shrinkage or necking-down. These tiny SFIs are difficult to be destroyed in the initial crushing stage, but they could be released in the final crushing stage together with the extraction of small PFIs. This hypothesis is supported by QMS analysis (Fig. 8a), which shows a significantly elevated fraction of H_2O, C_2H_6, and CH_4 in the final crushing stage, pointing to the breakdown of fine, alkane-bearing SFIs together with PFIs. As mineral micro-cracks might simultaneously capture $^{40}Ar_E$-rich geofluids and/or ^{40}Ar derived from country rocks or deep degassing process during rapid hydrothermal disturbance to form secondary fluid inclusions (Qiu and Wijbrans, 2006), these fine SFIs may contain excess argon. As a result, the $^{40}Ar/^{39}Ar$ stepwise crushing experiment yielded an increasing age plateau with older apparent ages for the final crushing stage (Fig. 6a).

A release of very fine SFIs together with PFIs in the last crushing steps of the cassiterite sample 13YGX36Cst was also suggested by the QMS stepwise crushing experiment (Fig. 8b, discussed in Section 5.1.3). The contribution of fine SFIs after sufficient crushing in the $^{40}Ar/^{39}Ar$ stepwise crushing experiment is reflected in the increase of $^{38}Ar_{Cl}$ proportions in the last several crushing steps (Fig. 8e). Given that careful hand-picking has ensured a low content of impurities in the cassiterite grains, and limited daughter minerals (solid phases grown from fluid), especially NaCl crystal, have been observed in the cassiterite sample, the higher $^{38}Ar_{Cl}$ proportions are unlikely derived from mineral impurities or daughter minerals. Instead, fine SFIs that formed during later hydrothermal disturbance are the most

possible source for the Cl (HCl or Cl_2) in the last crushing steps. These fine SFIs may also contain CO_2 and formamide and be released at the same time as Cl (Fig. 8b&e). As the $^{40}Ar/^{39}Ar$ crushing experiment (7080 drops in total) of the cassiterite sample ended before a significant release of these fine SFIs, whose significant release occurs after *ca.* 6691 drops based on the corresponding QMS crushing experiment (Fig. 8b), the limited argon derived from them is not enough to cause significant interference to the $^{40}Ar/^{39}Ar$ age derived from the PFIs.

On the other hand, the presence of CO_2 and organic molecules after sufficient crushing (e.g., around 10,000 drops) helped to reveal the provenance of the final stage gases, including argon, namely tiny mineral-hosted fluid inclusions. Argon is incompatible in most minerals (Roselieb et al., 1997; Kelley, 2002). The studied minerals, i.e., wolframite, cassiterite, and quartz, are not potassium-bearing minerals. Therefore, lattice-hosted argon or argon derived from *in situ* decay of lattice-hosted potassium should be negligible during $^{40}Ar/^{39}Ar$ crushing. Although experimental studies have suggested that argon could partition into minerals such as quartz, making it an effective sink for argon (Baxter, 2003; Watson and Cherniak, 2003; Thomas et al., 2008), higher solubility of argon in the mineral relative to those of the surrounding phases or high diffusivity of argon into the mineral is required for these minerals to have higher argon contents (Clay et al., 2010). In a fluid (fluid inclusion)-rich vein system, partition coefficients between minerals and fluids could be as low as 10^{-6} (Kelley, 2002), which indicates that fluid inclusions would dominate the argon budget in the mineral crystal. Experimental studies further demonstrate that the fluids, especially the vapor phases could act as the principal host and transport medium for argon in the C–H–O fluid bearing mineral crystal (Baxter, 2003; Watson and Cherniak, 2003). Therefore, during final stage crushing of the studied minerals, the predominant argon source should be the small fluid inclusions rather than argon in the mineral lattice, defects and/or dislocations. Additionally, grain-size analysis on the crushed mineral powders has revealed that the overwhelming majority of powders (crushed by a similar crusher of this study) have sizes larger than 1 μm after around ten thousand of pestle drops of crushing (Bai et al., 2013), from which we can infer that mineral lattices are unlikely quantitatively destroyed in the gentle $^{40}Ar/^{39}Ar$ stepwise crushing experiments (generally around or less than 10,000 pestle drops). Therefore, lattice-hosted argon is unlikely an important argon source during $^{40}Ar/^{39}Ar$ crushing, making this crushing technique applicable to date fluid inclusion bearing K-poor minerals.

6. CONCLUSIONS

In summary, building upon the model of fluid inclusion gas release systematics during gentle stepwise crushing experiments already established in previous studies (e.g., Qiu, 1996; Qiu and Wijbrans, 2006; Qiu and Jiang, 2007; Qiu et al., 2011; Jiang et al., 2012; Bai et al., 2013), our study demonstrates that the addition of QMS analyses provides important compositional information that greatly improves our ability to interpret $^{40}Ar/^{39}Ar$ geochronology data and obtain ages for different groups of fluid inclusions.

Several important conclusions are summarized below:

(1) Combined Raman spectroscopy and carbon isotope analyses indicate that the ore-forming fluids (i.e., primary fluid inclusions) of the Yaogangxian vein-type tungsten deposit are CH_4-rich and most likely associated with fluid-wall rock interactions, whereas the secondary fluid inclusions are generally CO_2-rich and probably derived from deep-seated sources.
(2) Compared with previous gas analysis of mixed gases extracted from the SFIs and PFIs by other crushing techniques, our technique of QMS measurements during gentle stepwise crushing can separate and distinguish the SFIs from the PFIs, and characterize their gas components separately. Stepwise crushing experiments suggest that gases trapped in microcracks and large-sized, vapor-rich secondary fluid inclusions, as well as large aqueous secondary fluid inclusions, are preferentially extracted in the earlier crushing stages. In contrast, a dominant release of the smaller primary fluid inclusions is observed in the final crushing stage.
(3) $^{40}Ar/^{39}Ar$ stepwise crushing experiments yielded ages of 128–127 Ma during the intermediate crushing stage, which are in accordance with the result of $^{40}Ar/^{39}Ar$ stepwise heating of late K-feldspar vein (129 Ma). This indicates a secondary hydrothermal event at *ca.* 129 Ma.
(4) The $^{40}Ar/^{39}Ar$ crushing experiments of wolframite, cassiterite and vein quartz yielded identical ages of 159–154 Ma during the final crushing stages, which agree well with the ore-forming ages established by many previous studies.
(5) The combined fluid inclusion QMS gas composition analyses and $^{40}Ar/^{39}Ar$ stepwise crushing can provide a better understanding of gas release patterns during crushing experiments. Our results further demonstrate that the gentle stepwise crushing technique can progressively extract different generations of fluid inclusions and the $^{40}Ar/^{39}Ar$ stepwise crushing technique has great potential in constraining the timing of different geofluid activities in general.

ACKNOWLEDGEMENTS

We thank the anonymous reviewers and the editors for their constructive comments and suggestions, which greatly improved the manuscript. The authors would also like to thank Julia M. Ribeiro, Da-Yong Tan, Ji-Bing Zhou, Rong-Qing Zhang, Jeremie Soldner and Cong Fang for the helpful comments on the manuscript. Our appreciation also goes to the engineers in Yaogangxian tungsten deposit for their assistance during sampling. This project is supported by the National Natural Science Foundation of China (No: 41630315, No: 91128203 & No: 41688103). A 100 Talents Program of the Chinese Academy of Sciences to Ying-De Jiang is also acknowledged. This is contribution IS-2657 from GIG-CAS.

APPENDIX A. SUPPLEMENTARY MATERIAL

Supplementary data to this article can be found online at https://doi.org/10.1016/j.gca.2019.02.016.

REFERENCES

Allard P. (1982) Stable isotope composition of hydrogen, carbon and sulphur in magmatic gases from rift and island arc volcanoes. *Bull. Volcanologique* **45**, 269–271.

Andrawes F., Holzer G., Roedder E., Gibson, Jr, E. K. and Oro J. (1984) Gas chromatographic analysis of volatiles in fluid and gas inclusions. *J. Chromatogr. A* **302**, 181–193.

Audétat A., Günther D. and Heinrich C. A. (1998) Formation of a magmatic-hydrothermal ore deposit: insights with LA-ICP-MS analysis of fluid inclusions. *Science* **279**, 2091–2094.

Azmy K. and Blamey N. J. F. (2013) Source of diagenetic fluids from fluid-inclusion gas ratios. *Chem. Geol.* **347**, 246–254.

Bai X. J., Jiang Y. D., Hu R. G., Gu X. P. and Qiu H. N. (2018a) Revealing mineralization and subsequent hydrothermal events: insights from $^{40}Ar/^{39}Ar$ isochron and novel gas mixing lines of hydrothermal quartzs by progressive crushing. *Chem. Geol.*, 332–341.

Bai X. J., Qiu H. N., Liu W. G. and Mei L. F. (2018b) Automatic $^{40}Ar/^{39}Ar$ dating techniques using multicollector ARGUS VI noble gas mass spectrometer with self-made peripheral apparatus. *J. Earth Sci.* **29**, 408–415.

Bai X. J., Wang M., Jiang Y. D. and Qiu H. N. (2013) Direct dating of tin-tungsten mineralization of the Piaotang tungsten deposit, South China, by ^{40}Ar–^{39}Ar progressive crushing. *Geochim. Cosmochim. Acta* **114**, 1–12.

Baxter E. F. (2003) Quantification of the factors controlling the presence of excess ^{40}Ar or ^{4}He. *Earth. Planet. Sci. Lett.* **216**, 619–634.

Blamey N. J. F. (2012) Composition and evolution of crustal, geothermal and hydrothermal fluids interpreted using quantitative fluid inclusion gas analysis. *J. Geochem. Explor.* **116–117**, 17–27.

Blank J. G., Delaney J. R. and Marais D. J. D. (1993) The concentration and isotopic composition of carbon in basaltic glasses from the Juan de Fuca Ridge, Pacific Ocean. *Geochim. Cosmochim. Acta* **57**, 875–887.

Campbell A. R. and Panter K. S. (1990) Comparison of fluid inclusions in coexisting (cogenetic?) wolframite, cassiterite, and quartz from St. Michael's Mount and Cligga Head, Cornwall, England. *Geochim. Cosmochim. Acta* **54**, 673–681.

Camprubí A., Chomiak B. A., Villanueva-Estrada R. E., Canals À., Norman D. I., Cardellach E. and Stute M. (2006) Fluid sources for the La Guitarra epithermal deposit (Temascaltepec district, Mexico): volatile and helium isotope analyses in fluid inclusions. *Chem. Geol.* **231**, 252–284.

Cao X. F., Lv X. B., He M. C., Niu H., Du B. F. and Mei W. (2009) An infrared microscope investigation of fluid inclusions in coexisting quartz and wolframite: a case study of Yaogangxian quartz-vein wolframite deposit. *Miner. Deposits* **28**, 611–620 (in Chinese with English abstract).

Charvet J., Shu L., Shi Y., Guo L. and Faure M. (1996) The building of south China: collision of Yangzi and Cathaysia blocks, problems and tentative answers. *J. SE Asian Earth Sci.* **13**, 223–235.

Chen Y. R. (1981) Geological features and ore-prospecting indications in the Yaogangxian vein-type tungsten deposit. *Geol. Prospect.* **17**, 25–30 (in Chinese with English abstract).

Chen Y. R. (1988) Geological and geochemical characteristics and diagenetic-minerogenetic processes of Yaogangxian granite. *Miner. Resour. Geol.* **2**, 62–72 (in Chinese with English abstract).

Clay P. L., Baxter E. F., Cherniak D. J., Kelley S. P., Thomas J. B. and Watson E. B. (2010) Two diffusion pathways in quartz: a combined UV-laser and RBS study. *Geochim. Cosmochim. Acta* **74**, 5906–5925.

Dai Y., Yu X., Wu G., Li C., Qiu J., Zhang J. and Luo P. (2011) Characteristics of sulfide minerals, genetic type and metallogenic epoch of the Caijiaping lead-zinc deposit, North Wuyi Area, Jiangxi Province. *Earth Sci. Front.* **18**, 321–338 (in Chinese with English abstract).

Deines P., Gold D. P., Deines P. and Gold D. P. (1973) Isotopic composition of carbonatite and kimberlite carbonates and their bearing on the isotopic composition of deep-seated carbon. *Geochim. Cosmochim. Acta* **37**, 1709–1733.

Diamond L. W., Tarantola A. and Stünitz H. (2010) Modification of fluid inclusions in quartz by deviatoric stress. II: experimentally induced changes in inclusion volume and composition. *Contrib. Mineral. Petrol.* **160**, 825–843.

Dong S. H., Bi X. W., Hu R. Z., Chen Y. W. and Chen H. (2011) Characteristics of ore-forming fluid in yaogangxian quartz-vein wolframite deposit, Hunan Province. *J. Mineral. Petrol.* **31**, 54–60 (in Chinese with English abstract).

Frost R. L., Kristóf J., Horváth E. and Kloprogge J. T. (2001) Raman microscopy of formamide-intercalated kaolinites treated by controlled-rate thermal analysis technology. *J. Raman Spectrosc.* **32**, 873–880.

Fu J. M., Ma L. Y., Cheng S. B. and Lu Y. Y. (2013) Metallogenesis of W(Sn) deposits and their exploration in nanling range, China. *Geol. J. China Univ.* **19**, 202–212 (in Chinese with English abstract).

Giuliani G., Li Y. D. and Sheng T. F. (1988) Fluid inclusion study of Xihuashan tungsten deposit in the southern Jiangxi province, China. *Miner. Deposita* **23**, 24–33.

Graney J. R. and Kesler S. E. (1995) Factors affecting gas analysis of inclusion fluid by quadrupole mass spectrometry. *Geochim. Cosmochim. Acta* **59**, 3977–3986.

Hinrichs K. U., Hayes J. M., Bach W., Spivack A. J., Hmelo L. R., Holm N. G., Johnson C. G. and Sylva S. P. (2006) Biological formation of ethane and propane in the deep marine subsurface. *PNAS* **103**, 14684–14689.

Hoefs J. (2009) *Stable Isotope Geochemistry*. Springer, Berlin.

Horita J. and Berndt M. E. (1999) Abiogenic methane formation and isotopic fractionation under hydrothermal conditions. *Science* **285**, 1055–1057.

Hu R. G., Wijbrans J., Brouwer F., Zhao L. H., Wang M. and Qiu H. N. (2015) Retrograde metamorphism of the eclogite in North Qaidam, western China: constraints by joint $^{40}Ar/^{39}Ar$ in vacuo crushing and stepped heating. *Geosci. Front.* **6**, 759–770.

Jenden P. D., Kaplan I. R., Hilton D. R. and Craig H. (1993) Abiogenic hydrocarbons and mantle helium in oil and gas fields. In The Future of Energy Gases (ed. D. G. Howell). United States Geological Survey, Professional Paper (United States). pp. 31–56.

Jiang Y. D., Qiu H. N. and Xu Y. G. (2012) Hydrothermal fluids, argon isotopes and mineralization ages of the Fankou Pb-Zn deposit in south China: insights from sphalerite $^{40}Ar/^{39}Ar$ progressive crushing. *Geochim. Cosmochim. Acta* **84**, 369–379.

Kawagucci S., Ueno Y., Takai K., Toki T., Ito M., Inoue K., Makabe A., Yoshida N., Muramatsu Y. and Takahata N. (2013) Geochemical origin of hydrothermal fluid methane in sediment-associated fields and its relevance to the geographical distribution of whole hydrothermal circulation. *Chem. Geol.* **339**, 213–225.

Ke Y. K. (1998) *Handbook of Analytical Chemistry (Part III): Spectral Analysis*, second ed. Chemical Industry Press, Beijing.

Kelley S. (2002) Excess argon in K-Ar and Ar–Ar geochronology. *Chem. Geol.* **188**, 1–22.

Kelley S., Turner G., Butterfield A. W. and Shepherd T. J. (1986) The source and significance of argon isotopes in fluid inclusions from areas of mineralization. *Earth. Planet. Sci. Lett.* **79**, 303–318.

Kendrick M. A., Honda M., Walshe J. and Petersen K. (2011) Fluid sources and the role of abiogenic-CH_4 in Archean gold mineralization: constraints from noble gases and halogens. *Precambr. Res.* **189**, 313–327.

Kendrick M. A., Miller J. M. and Phillips D. (2006) Part II. Evaluation of ^{40}Ar–^{39}Ar quartz ages: implications for fluid inclusion retentivity and determination of initial $^{40}Ar/^{36}Ar$ values in Proterozoic samples. *Geochim. Cosmochim. Acta* **70**, 2562–2576.

Koppers A. A. P. (2002) ArArCALC—software for $^{40}Ar/^{39}Ar$ age calculations. *Comput. Geosci.* **28**, 605–619.

Landis G. P., Snee L. W. and Juliani C. (2005) Evaluation of argon ages and integrity of fluid-inclusion compositions: stepwise noble gas heating experiments on 1.87 Ga alunite from Tapajós Province, Brazil. *Chem. Geol.* **215**, 127–153.

Lecumberrisanchez P., Vieira R., Heinrich C. A., Pinto F. and Wälle M. (2017) Fluid-rock interaction is decisive for the formation of tungsten deposits. *Geology* **45**, 579–582.

Lees A. J., Straughan B. P. and Gardiner D. J. (1981) Electrolyte—formamide interactions studied by raman spectroscopy. *J. Mol. Struct.* **71**, 61–70.

Li S. T., Wang J. B., Zhu X. Y., Wang Y. L., Han Y. and Guo N. N. (2011) Chronological characteristics of the Yaogangxian composite pluton in Hunan Province. *Geol. Expl.* **47**, 143–150 (in Chinese with English abstract).

Li S. T., Zhu X. Y., Wang J. B., Wang Y. L., Cheng X. Y. and Jiang B. B. (2015) Geological and geochemical characteristics of the Yaogangxian complex grantoid and its relationship with tungsten mineralization. *Miner. Exploration* **6**, 347–355 (in Chinese with English abstract).

Li W. S., Ni P., Pan J. Y., Wang G. G., Chen L. L., Yang Y. L. and Ding J. Y. (2017) Fluid inclusion characteristics as an indicator for tungsten mineralization in the Mesozoic Yaogangxian tungsten deposit, central Nanling district, South China. *J. Geochem. Explor.* **192**, 1–17.

Li X. H., Li W. X., Li Z. X., Lo C. H., Wang J., Ye M. F. and Yang Y. H. (2009) Amalgamation between the Yangtze and Cathaysia Blocks in South China: constraints from SHRIMP U-Pb zircon ages, geochemistry and Nd-Hf isotopes of the Shuangxiwu volcanic rocks. *Precambr. Res.* **174**, 117–128.

Li X. H. and Mcculloch M. T. (1996) Secular variation in the Nd isotopic composition of Neoproterozoic sediments from the southern margin of the Yangtze Block: evidence for a Proterozoic continental collision in southeast China. *Precambr. Res.* **76**, 67–76.

Li Z. X. and Li X. H. (2007) Formation of the 1300-km-wide intracontinental orogen and postorogenic magmatic province in Mesozoic South China: a flat-slab subduction model. *Geology* **35**, 179–182.

Liu M., Qiu H. N., Bai X. J., Xiao M. and He L. Y. (2015) Fluid inclusion studies of Xitian tin-tungsten polymetallic deposit in Hunan Province. *Miner. Deposits* **34**, 981–998 (in Chinese with English abstract).

Lowenstern J. B. (1995) Application of silicate-melt inclusions to the study of magmatic volatiles. In *Magmas, Fluids, and Ore Deposits* (ed. J. F. H. Thompson). Mineral. Assoc. Can, Nepean, Ontario, Canada, pp. 71–99.

Lüders V. and Plessen B. (2015) Stable carbon isotope ratios of CH_4-rich gas inclusions in shale-hosted fracture-fill mineralization: a tool for tracing hydrocarbon generation and migration in shale plays for oil and gas. *Mar. Pet. Geol.* **63**, 68–81.

Lüders V., Plessen B. and di Primio R. (2012) Stable carbon isotopic ratios of CH_4–CO_2-bearing fluid inclusions in fracture-fill mineralization from the Lower Saxony Basin (Germany) – a tool for tracing gas sources and maturity. *Mar. Pet. Geol.* **30**, 174–183.

Mao J., Xie G., Guo C. and Chen Y. (2007) Large-scale tungsten-tin mineralization in the Nanling region, South China: metallogenic ages and corresponding geodynamic processes. *Acta Petrol. Sin.* **23**, 2329–2338 (in Chinese with English abstract).

Mao J. W., Chen M. H. and Yuan S. D. (2011) Geological characteristics of the Qinhang (or Shihang) Metallogenic Belt in South China and spatial-temporal distribution regularity of mineral deposits. *Acta Geol. Sin.* **85**, 636–658 (in Chinese with English abstract).

Matsumoto T., Chen Y. and Matsuda J. I. (2001) Concomitant occurrence of primordial and recycled noble gases in the Earth's mantle. *Earth. Planet. Sci. Lett.* **185**, 35–47.

McCollom T. M. (2008) Observational, experimental, and theoretical constraints on carbon cycling in mid-ocean ridge hydrothermal systems. In *Magma to Microbe: Modeling Hydrothermal Processes at Ocean Spreading Centers. Geophysical Monograph Series* (eds. R. P. Lowell, J. S. Seewald, A. Metaxas and M. R. Perfit). American Geophysical Union, pp. 193–213.

Melluso L., De'Gennaro R., Fedele L., Franciosi L. and Morra V. (2012) Evidence of crystallization in residual, Cl-F-rich, agpaitic, trachyphonolitic magmas and primitive Mg-rich basalt-trachyphonolite interaction in the lava domes of the Phlegrean Fields (Italy). *Geol. Mag.* **149**, 532–550.

Moore J. N., Norman D. I. and Kennedy B. M. (2001) Fluid inclusion gas compositions from an active magmatic-hydrothermal system: a case study of the Geysers geothermal field, USA. *Chem. Geol.* **173**, 3–30.

Morishita Y. (1991) Fluid evolution and geobarometry on the Ohtani and Kaneuchi tungsten-quartz vein deposits, Japan: oxygen and carbon isotopic evidence. *Miner. Deposita* **26**, 40–50.

Naumov V. B., Tolstykh M. L., Grib E. N., Leonov V. L. and Kononkova N. N. (2008) Chemical composition, volatile components, and trace elements in melts of the Karymskii volcanic center, Kamchatka, and Golovnina volcano, Kunashir Island: evidence from inclusions in minerals. *Petrology* **16**, 1–18.

Ni P., Wang X. D., Wang G. G., Huang J. B., Pan J. Y. and Wang T. G. (2015) An infrared microthermometric study of fluid inclusions in coexisting quartz and wolframite from Late Mesozoic tungsten deposits in the Gannan metallogenic belt, South China. *Ore Geol. Rev.* **65**(Part 4), 1062–1077.

Niedermann S. and Bach W. (1998) Anomalously nucleogenic neon in North Chile Ridge basalt glasses suggesting a previously degassed mantle source. *Earth Planet Sci. Lett.* **160**, 447–462.

Norman D. I. and Moore J. N. (1999) Methane and excess N_2 and Ar in geothermal fluid inclusions. In *Proceedings: Twenty-fourth Workshop of Geothermal Reservoir Engineering*. Stanford University, Stanford, California, pp. 233–240.

Norman D. I. and Musgrave J. A. (1994) N_2-Ar-He compositions in fluid inclusions: indicators of fluid source. *Geochim. Cosmochim. Acta* **58**, 1119–1131.

Norman D. I. and Sawkins F. J. (1987) Analysis of volatiles in fluid inclusions by mass spectrometry. *Chem. Geol.* **61**, 1–10.

O'Nions R. and Ballentine C. (1993) Rare gas studies of basin scale fluid movement. *Phil. Trans. R. Soc. Lond. A* **344**, 141–156.

Okada T., Itaya T., Sato M. and Nagao K. (1994) Noble gas isotopic composition of deep underground water in Osaka plain, central Japan: evidence for mantle He and model for new volcanism. *Isl. Arc* **3**, 221–231.

Ozima M. and Podosek F. A. (1983) *Noble Gas Geochemistry*. Cambridge University Press, New York.

Ozima M., Zashu S., Takigami Y. and Turner G. (1989) Origin of the anomalous ^{40}Ar–^{39}Ar age of Zaire cubic diamonds-Excess ^{40}Ar in pristine mantle fluids. *Nature* **337**, 226–229.

Peng J. T., Zhou M. F., Hu R. Z., Shen N. P., Yuan S. D., Bi X. W., Du A. D. and Qu W. J. (2006) Precise molybdenite Re–Os and mica Ar–Ar dating of the Mesozoic Yaogangxian tungsten deposit, central Nanling district, South China. *Miner. Deposita* **41**, 661–669.

Pettke T., Frei R., Kramers J. D. and Villa I. M. (1997) Isotope systematics in vein gold from Brusson, Val d'Ayas (NW Italy) 3. (U + Th)He and K/Ar in native Au and its fluid inclusions. *Chem. Geol.* **135**, 173–187.

Pironon J., Pagel M., Lévêque M. H. and Mogé M. (1995) Organic inclusions in salt. Part I: Solid and liquid organic matter, carbon dioxide and nitrogen species in fluid inclusions from the Bresse basin (France). *Org. Geochem.* **23**, 391–402.

Potter J., Salvi S. and Longstaffe F. J. (2013) Abiogenic hydrocarbon isotopic signatures in granitic rocks: identifying pathways of formation. *Lithos* **182–183**, 114–124.

Puranik P. G. and Ramiah K. V. (1959) Infrared and Raman spectroscopic studies of the association of formamide. *J. Mol. Spectrosc.* **3**, 486–495.

Qiu H. N. (1996) ^{40}Ar–^{39}Ar dating of the quartz samples from two mineral deposits in western Yunnan (SW China) by crushing in vacuum. *Chem. Geol.* **127**, 211–222.

Qiu H. N. and Dai T. M. (1989) $^{40}Ar/^{39}Ar$ technique for dating the fluid Inclusions of quartz from a hydrothermal deposit. *Chin. Sci. Bull.* **34**, 1887–1890.

Qiu H. N. and Jiang Y. D. (2007) Sphalerite $^{40}Ar/^{39}Ar$ progressive crushing and stepwise heating techniques. *Earth. Planet. Sci. Lett.* **256**, 224–232.

Qiu H. N. and Wijbrans J. R. (2006) Paleozoic ages and excess ^{40}Ar in garnets from the Bixiling eclogite in Dabieshan, China: new insights from $^{40}Ar/^{39}Ar$ dating by stepwise crushing. *Geochim. Cosmochim. Acta* **70**, 2354–2370.

Qiu H. N. and Wijbrans J. R. (2008) The Paleozoic metamorphic history of the Central Orogenic Belt of China from $^{40}Ar/^{39}Ar$ geochronology of eclogite garnet fluid inclusions. *Earth Planet. Sci. Lett.* **268**, 501–514.

Qiu H. N., Wijbrans J. R., Brouwer F. M., Yun J. B., Zhao L. H. and Xu Y. G. (2010) Amphibolite facies retrograde metamorphism of the Zhujiachong eclogite, SE Dabieshan: $^{40}Ar/^{39}Ar$ age constraints from argon extraction using UV-laser microprobe, in vacuo crushing and stepwise heating. *J. Metamorph. Geol.* **28**, 477–487.

Qiu H. N., Wu H. Y., Yun J. B., Feng Z. H., Xu Y. G., Mei L. F. and Wijbrans J. R. (2011) High-precision ^{40}Ar–^{39}Ar age of the gas emplacement into the Songliao Basin. *Geology* **39**, 451–454.

Qiu H. N., Zhu B. Q. and Sun D. Z. (2002) Age significance interpreted from ^{40}Ar–^{39}Ar dating of quartz samples from the Dongchuan Copper Deposits, Yunnan, SW China, by crushing and heating. *Geochem. J.* **36**, 475–491.

Roedder E. (1984) *Fluid Inclusions*. Mineralogical Society of America.

Roedder E. (1992) Fluid inclusion evidence for immiscibility in magmatic differentiation ☆. *Geochim. Cosmochim. Acta* **56**, 5–20.

Roselieb K., Blanc P., Büttner H., Jambon A., Rammensee W., Rosenhauer M., Vielzeuf D. and Walter H. (1997) Experimental study of argon sorption in quartz: evidence for argon incompatibility. *Geochim. Cosmochim. Acta* **61**, 533–542.

Schoell M. (1988) Multiple origins of methane in the Earth. *Chem. Geol.* **71**, 1–10.

Seitz J. C., Pasteris J. D. and Chou I. M. (1996) Raman spectroscopic characterization of gas mixtures; II, Quantitative composition and pressure determination of the CO_2-CH_4 system. *Am. J. Sci.* **296**, 577–600.

Shepherd T. J. and Darbyshire D. P. F. (1981) Fluid inclusion Rb–Sr isochrons for dating mineral deposits. *Nature* **290**, 578–579.

Shepherd T. J. and Miller M. F. (1988) Fluid inclusion volatiles as a guide to tungsten deposits, Southwest England: application to other Sn-W provinces in Western Europe. In *Mineral Deposits within the European Community*. Springer, Berlin Heidelberg, pp. 29–52.

Shepherd T. J., Rankin A. H. and Alderton D. H. M. (1985) *A practical guide to fluid inclusion studies*. Distributed in the USA by Chapman and Hall, Glasgow, New York.

Shu L. S. (2007) *Geological Setting of the Nanling Range*. Science Press, Beijing.

Singh T. B., Rey L. and Gartia R. K. (2011) Applications of PeakFit software in thermoluminescence studies. *Indian J. Pure Appl. Phys.* **49**, 297–302.

Steiger R. H. and Jäger E. (1977) Subcommission on geochronology: convention on the use of decay constants in geo-and cosmochronology. *Earth Planet. Sci. Lett.* **36**, 359–362.

Taran Y. A., Kliger G. A. and Sevastianov V. S. (2007) Carbon isotope effects in the open-system Fischer-Tropsch synthesis. *Geochim. Cosmochim. Acta* **71**, 4474–4487.

Thomas J. B., Cherniak D. J. and Watson E. B. (2008) Lattice diffusion and solubility of argon in forsterite, enstatite, quartz and corundum. *Chem. Geol.* **253**, 1–22.

Turner G. (1988) Hydrothermal fluids and argon isotopes in quartz veins and cherts ☆. *Geochim. Cosmochim. Acta* **52**, 1443–1448.

Turner G. and Bannon M. P. (1992) Argon isotope geochemistry of inclusion fluids from granite-associated mineral veins in southwest and northeast England*. *Geochim. Cosmochim. Acta* **56**, 227–243.

Turner G. and Wang S. S. (1992) Excess argon, crustal fluids and apparent isochrons from crushing K-feldspar. *Earth Planet. Sci. Lett.* **110**, 193–211.

Uunk B., Postma O., Wijbrans J. and Brouwer F. (2017) Direct 40Ar/39Ar age determination of fluid inclusions using in-vacuo stepwise crushing-Example of garnet from the Cycladic Blueschist Unit on Syros. EGU General Assembly Conference.

Van Den Kerkhof A. M. and Hein U. F. (2001) Fluid inclusion petrography. *Lithos* **55**, 27–47.

Vetrin V. R., Kamenskii I. L. and Ikorskii S. V. (2007) Helium and argon isotopes in lower crustal xenoliths from the belomorian mobile belt. *Petrology* **15**, 302–313.

Villa I. M. (2001) Radiogenic isotopes in fluid inclusions. *Lithos* **55**, 115–124.

Wang M., Bai X. J., Hu R. G., Cheng S. B., Pu Z. P. and Qiu H. N. (2015) Direct dating of cassiterite in Xitian tungsten-tin polymetallic deposit, south-east Hunan, by $^{40}Ar/^{39}Ar$ progressive crushing. *Geotecton. Metallog.* **39**, 1049–1060 (in Chinese with English abstract).

Wang M., Bai X. J., Yun J. B., Zhao L. H., Li Y. L., Wang Z. Y., Pu Z. P. and Qiu H. N. (2016) $^{40}Ar/^{39}Ar$ dating of mineralization of Shizhuyuan polymetallic deposit. *Geochimica* **45**, 41–51 (in Chinese with English abstract).

Wang S. S. (1983) Age determinations of ^{40}Ar–^{40}K, ^{40}Ar–^{39}Ar and radiogenic ^{40}Ar released characteristics on K-Ar geostandards of China. *Chin. J. Geol.*, 315–323 (in Chinese with English abstract).

Wang Y. L., Pei R. F., Li J. W., Qu W. J., Li L., Wang H. L. and Du A. D. (2010) Re–Os dating of molybdenite from the Yaogangxian tungsten deposit, South China, and its geological significance. *Acta Geol. Sin. – English Ed.* **82**, 820–825.

Watson E. B. and Cherniak D. J. (2003) Lattice diffusion of Ar in quartz, with constraints on Ar solubility and evidence of nanopores. *Geochim. Cosmochim. Acta* **67**, 2043–2062.

Wei W., Hu R., Bi X., Peng J., Su W., Song S. and Shi S. (2012) Infrared microthermometric and stable isotopic study of fluid inclusions in wolframite at the Xihuashan tungsten deposit, Jiangxi province, China. *Miner. Deposita* **47**, 589–605.

Whiticar M. J. (1999) Carbon and hydrogen isotope systematics of bacterial formation and oxidation of methane. *Chem. Geol.* **161**, 291–314.

Yu Z. F., Xu H., Zhu X. Y., Wang Y. L. and Cheng X. Y. (2015) Characteristics and evolution of ore-forming fluids in Yaogangxian tungsten deposit, Hunan Province. *Miner. Deposits* **34**, 309–320 (in Chinese with English abstract).

Zhang L. G. (1987) Oxygen isotope studies of wolframite in tungsten ore deposits of south China. *Chin. J. Geochem.* **7**, 109–119 (in Chinese with English abstract).

Zhou X. and Li W. (2000) Origin of Late Mesozoic igneous rocks in Southeastern China: implications for lithosphere subduction and underplating of mafic magmas. *Tectonophysics* **326**, 269–287.

Zhou X., Sun T., Shen W., Shu L. and Niu Y. (2006) Petrogenesis of Mesozoic granitoids and volcanic rocks in South China: a response to tectonic evolution. *Episodes* **29**, 26–33.

Zhu X. Y., Wang J. B., Wang Y. L., Cheng X. Y. and Fu Q. B. (2014a) Relative closed ore-forming in the tungsten-bearing quartz vein: a case study of the Yaogangxian, Hunan Province. *Acta Geol. Sin.* **88**, 825–835 (in Chinese with English abstract).

Zhu X. Y., Wang J. B., Wang Y. L., Cheng X. Y., Fu Q. B., Fu M. and Yu Z. F. (2014b) Characteristics of Stable Isotopes S, Pb, O and H isotopes in the Yaogangxian Tungsten Deposits, Hunan Province. *Geol. Expl.* **50**, 947–960 (in Chinese with English abstract).

Zhu X. Y., Wang Y. L., Cheng X. Y., Tian Y., Fu Q., Li S. and Yu Z. (2015) Metallogenic system of Yaogangxian quartz vein-type tungsten deposit, Hunan Province. *Miner. Deposits* **34**, 874–894 (in Chinese with English abstract).

Associate editor: Chris M. Hall